

Non-Abelian hyperbolic band theory from supercells

Patrick M. Lenggenhager ^{1,2,3,4,*}, Joseph Maciejko ^{4,5,†} and Tomáš Bzdušek ^{1,2,‡}

¹Department of Physics, University of Zurich, Winterthurerstrasse 190, 8057 Zurich, Switzerland

²Condensed Matter Theory Group, Paul Scherrer Institute, 5232 Villigen PSI, Switzerland

³Institute for Theoretical Physics, ETH Zurich, 8093 Zurich, Switzerland

⁴Theoretical Physics Institute, University of Alberta, Edmonton, Alberta T6G 2E1, Canada

⁵Department of Physics, University of Alberta, Edmonton, Alberta T6G 2E1, Canada

(Dated: January 18, 2024)

Wave functions on periodic lattices are commonly described by Bloch band theory. Besides Abelian Bloch states labeled by a momentum vector, hyperbolic lattices support non-Abelian Bloch states that have so far eluded analytical treatments. By adapting the solid-state-physics notions of supercells and zone folding, we devise a method for the systematic construction of non-Abelian Bloch states. The method applies Abelian band theory to sequences of supercells, recursively built as symmetric aggregates of smaller cells, and enables a rapidly convergent computation of bulk spectra and eigenstates for both gapless and gapped tight-binding models. Our supercell method provides an efficient means of approximating the thermodynamic limit and marks a pivotal step towards a complete band-theoretic characterization of hyperbolic lattices.

Introduction.— Hyperbolic lattices are uniform discretizations of the two-dimensional (2D) *hyperbolic plane* with constant negative curvature. Recent experimental realizations in metamaterials, including coplanar-waveguide resonator [1] and electric-circuit networks [2], have elevated them from objects of academic interest to building blocks for engineering metamaterials. These advances have sparked a renewed interest in condensed-matter models on hyperbolic lattices, both in theory [3–20] and experiment [21–25]. The fundamental construction involves *regular tessellations*, where q copies of regular p -gons meet at each vertex, denoted by $\{p, q\}$ in Schläfli notation, with $(p - 2)(q - 2) > 4$.

For Euclidean lattices, Bloch’s theorem labels Hamiltonian eigenstates by irreducible representations (IRs) of the translation group and enables a description in terms of a unit cell together with reciprocal space. While Bloch’s theorem has been generalized [26–33] to hyperbolic lattices, this comes with fundamental difficulties. First, Bloch’s theorem requires periodic boundary conditions (PBC), but constructing finite PBC *clusters* that approximate the thermodynamic limit is highly nontrivial [27, 34, 35]. Second, Euclidean translation groups are Abelian, such that only 1D IRs exist. In contrast, hyperbolic translation groups admit higher-dimensional IRs; therefore, hyperbolic band theory (HBT) requires *non-Abelian* Bloch states besides the usual Abelian ones [27]. We here refer to the approximation that considers only 1D IRs as *Abelian* HBT (AHBT) [26].

To deal with these difficulties, various avenues have been explored. Finite *flakes* with open boundary conditions exhibit a macroscopic fraction of boundary sites, which is advantageous when interested in boundary effects [10, 15–17], but challenging when studying bulk properties. Good agreement of AHBT with bulk-projected spectra on flakes is observed in some models [10–12], but crucial features are missed in others [36]. Very recently, Lux and Prodan [34, 35] have shown

how to choose increasingly large PBC clusters to achieve convergence to the thermodynamic limit, while Mosseri and Vidal [37] have computed the density of states (DOS) of gapless models using a continued-fraction method. However, neither provides a reciprocal-space description, i.e., a description in terms of bulk states of the infinite lattice labeled by translation quantum numbers.

In this work, we introduce the *supercell method* to gain systematic access to non-Abelian Bloch states using AHBT combined with particular sequences of PBC clusters. We construct such sequences for various hyperbolic $\{p, q\}$ lattices using results from geometric group theory [38]. We observe rapid convergence of the DOS to the thermodynamic limit for various models. Our approach is computationally more efficient than real-space methods and affords the conceptual advantages of labeling eigenstates by momenta. We implement our algorithms in an open-source software package [39] for the computational algebra system GAP [40].

Supercells.— A lattice consists of copies of some chosen unit cell, generated by discrete translations forming a translation group Γ . While one commonly chooses a smallest *primitive cell*, implying a maximal translation group $\Gamma^{(1)}$, one can instead consider a *supercell*, i.e., a collection of multiple primitive cells. Accordingly, only a subgroup $\Gamma^{(2)}$ of translations $\Gamma^{(1)}$ is required to generate the lattice. An example pair of primitive cell and supercell of the (Euclidean) $\{4, 4\}$ lattice and the (hyperbolic) $\{8, 8\}$ lattice is illustrated in Figs. 1a and 1b, respectively.

Dividing the lattice into copies of a chosen cell facilitates PBC, where the lattice is compactified on a closed manifold by identifying sides related by certain translations. On Euclidean lattices, such *PBC clusters* provide an approximation of the infinite lattice with well-converging bulk properties [42]. To implement PBC on a single cell, opposite sides are identified and the cell is compactified on a torus—independent of its size (Fig. 1c). In contrast, due to the negative curvature, hyperbolic PBC clusters are compactified on manifolds of genus $g \geq 2$ [43]. According to the Riemann-Hurwitz formula [44], the genus g_{sc} of a compactified supercell grows linearly with

* plengg@pks.mpg.de

† maciejko@ualberta.ca

‡ tomas.bzusek@uzh.ch

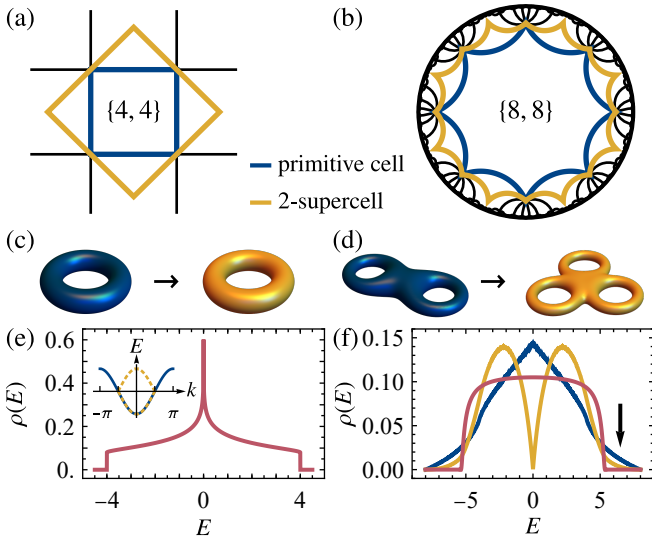


FIG. 1. Supercell construction for (a,c,e) the Euclidean $\{4,4\}$ and (b,d,f) hyperbolic $\{8,8\}$ lattice. (a,b) Primitive cell (blue) and symmetrized 2-supercell (yellow). (c,d) Compactified cells in real space. (e) Density of states ρ of the nearest-neighbor hopping model on the $\{4,4\}$ lattice as a function of energy E showing the characteristic van Hove singularity. The inset shows the momentum-space dispersion for the primitive cell (solid blue line) and for the supercell (yellow dashed line). (f) Density of Abelian Bloch states of the nearest-neighbor hopping model on the $\{8,8\}$ lattice for the primitive cell (blue), for the 2-supercell (yellow), and schematic extrapolation (for details see Supplemental Material [41]) to large supercells (red). The black arrow indicates a suppression near the band edges (see text).

the number N of primitive cells:

$$g_{sc} - 1 = N(g_{pc} - 1), \quad (1)$$

where g_{pc} is the genus of the compactified primitive cell. For the $\{8,8\}$ lattice, the primitive cell is compactified on a genus-2 surface, and the two-unit-cell supercell (2-supercell) on a genus-3 surface (Fig. 1d).

Translation symmetry further enables a reciprocal-space description of the infinite lattice, considering not just a single PBC cluster but also all of its translation-related copies. The choice of cell affects the reciprocal-space description. To illustrate this, consider nearest-neighbor (NN) hopping models on the $\{4,4\}$ and $\{8,8\}$ lattices with Hamiltonian $\mathcal{H} = -\sum_{\langle i,j \rangle} c_i^\dagger c_j$, where $\langle i,j \rangle$ denotes NNs. For Euclidean lattices, the Brillouin zone (BZ) is reduced due to the enlargement of the cell, leading to band folding (Fig. 1e, inset); nevertheless, the computed DOS is independent of the cell size. By contrast, in the hyperbolic case, the density of Abelian Bloch states changes significantly when going from a primitive cell to a 2-supercell (Fig. 1f). However, below and in the Supplemental Material [41], we demonstrate that the DOS converges with increasing supercell size.

Real-space perspective.— The symmetries of a $\{p,q\}$ lattice are captured [28, 45] by the *triangle group* Δ generated by reflections a, b, c across the sides of a triangle, called *Schwarz triangle*, with internal angles $\frac{2\pi}{r}$ (with $r=2$), $\frac{2\pi}{q}$, and $\frac{2\pi}{p}$

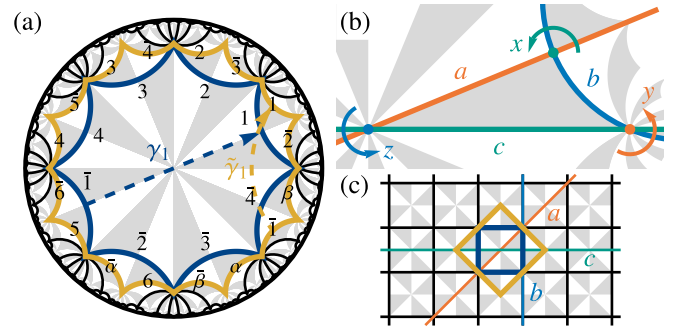


FIG. 2. Symmetries of hyperbolic lattices. (a) $\{8,8\}$ lattice (black lines) with the triangle group $\Delta(2,8,8)$ as space group (indicated by gray/white triangles). The primitive cell (blue polygon) and 2-supercell (yellow polygon) and their edge identifications are shown: the edge $\bar{1}$ is related to 1 by the translation generator γ_1 ($\tilde{\gamma}_1$ for the supercell). Edges related by composite translations are labeled by α and β [41]. (b) Fundamental Schwarz triangle (gray) with reflections a, b, c across the edges of the triangle and rotations $x = ab, y = bc, z = ca$ around the vertices. (c) Square lattice with primitive cell, supercell, triangle group $\Delta(2,4,4)$, and reflection lines a, b, c .

(Figs. 2b and 2c). This is reflected in its *presentation*

$$\Delta(r, q, p) = \langle a, b, c | a^2, b^2, c^2, (ab)^r, (bc)^q, (ca)^p \rangle \quad (2)$$

with the *relators*, appearing to the right of the vertical line, set to the identity. Under the action of Δ , copies of the *fundamental Schwarz triangle* s_f tile the whole plane (see Figs. 2a and 2c for the $\{8,8\}$ and $\{4,4\}$ lattices, respectively). Formally, the abstract set S of all Schwarz triangles is the orbit of s_f under right action of Δ : $S = s_f \cdot \Delta$.

Interpreted as a space group, Δ encompasses point-group operations and translations. While the point group is generally not a subgroup of Δ (even in Euclidean lattices), translations form a *normal subgroup* $\Gamma \triangleleft \Delta$ [46], i.e., any translation conjugated by a reflection or rotation is again a translation. Indeed, Γ is usually defined [12, 28] as the largest *torsion-free* normal subgroup of orientation-preserving elements of Δ , where torsion-freeness captures the absence of elements of finite order in translation groups. Since $\Gamma \triangleleft \Delta$, the quotient Δ/Γ forms a group and plays the role of the point group. The transversal $T_\Delta(\Gamma)$ is a specific set of representatives of Δ/Γ .

The choice of Γ defines the cell, which comprises a finite number of Schwarz triangles (Fig. 2a) and therefore corresponds to a subset $C \subset S$ such that: (i) none of the elements are related by translations, and (ii) the right action of Γ on C recovers S , i.e., $S = C \cdot \Gamma$. The coset decomposition $\Delta = \bigcup_{t \in T_\Delta(\Gamma)} \Gamma t$ implies that $C = s_f \cdot T_\Delta(\Gamma)$. Different choices of $T_\Delta(\Gamma)$ lead to cells C differing in connectedness and symmetry. Our algorithms [39] take Δ/Γ as input, construct random and (for sufficiently small quotients) connected symmetric cells, and extract boundary identifications.

Our *supercell method* is a natural and systematic way to form sequences of PBC clusters suited to a reciprocal-space interpretation. We construct increasingly larger supercells, by recursively accreting smaller (super)cells in a symmetric fashion, starting with a single primitive cell. This results in a

nested sequence of finite-index normal subgroups,

$$\Gamma^{(1)} \triangleright \Gamma^{(2)} \triangleright \dots \triangleright \Gamma^{(m)} \triangleright \dots, \quad (3)$$

where $\Gamma^{(m)} \triangleleft \Delta$ for all m implies normality of the subgroup relationships in Eq. (3). Although there is a unique plane-filling hyperbolic $\{p, q\}$ lattice, the PBC clusters can have different infinite-size limits [27], indicating the choice of sequence is crucial. Recently, Lux and Prodan [34, 35] proposed a similar condition with the additional constraint $\bigcap_{m \geq 1} \Gamma^{(m)} = \{1\}$ and argued that such sequences lead to a well-defined thermodynamic limit [47]. Based on our results, we conjecture that the supercell sequences can be extended in a way that satisfies that additional constraint. While the supercell method does not give a unique sequence, we anticipate that all valid sequences converge to the same limit, consistent with our observations [41].

Translation symmetry allows us to define hopping models by specifying only the hopping amplitudes $h^{uv}(\gamma)$ from site v in the primitive cell $C^{(1)}$ to site u in the primitive cell translated by $\gamma \in \Gamma^{(1)}$. [Here $C^{(m)}$ is the cell associated with the translation group $\Gamma^{(m)}$, and $N^{(m)} = |\Gamma^{(1)}/\Gamma^{(m)}|$ counts primitive cells in $C^{(m)}$.] We additionally subdivide the lattice into copies of the $N^{(m)}$ -supercell $C^{(m)}$, so that the $N^{(m)}$ copies of $C^{(1)}$ in $C^{(m)}$ are generated by the quotient group $\Gamma^{(1)}/\Gamma^{(m)}$. By the coset decomposition, copies of the primitive cell are specified by $\eta_i \tilde{\gamma}$ with transversal elements $\eta_i \in T_{\Gamma^{(1)}}(\Gamma^{(m)})$ and $\tilde{\gamma} \in \Gamma^{(m)}$, and the most general translation-invariant hopping model takes the form [41],

$$\mathcal{H} = \sum_{\substack{\tilde{\gamma}, \tilde{\gamma}' \in \Gamma^{(m)} \\ \eta_i, \eta_j \in T_{\Gamma^{(1)}}(\Gamma^{(m)})}} \sum_{u, v} h^{uv} \left(\eta_i \tilde{\gamma} \tilde{\gamma}'^{-1} \eta_j^{-1} \right) c_{\eta_i \tilde{\gamma}}^u c_{\eta_j \tilde{\gamma}'}^v, \quad (4)$$

where $\eta_i \tilde{\gamma} \tilde{\gamma}'^{-1} \eta_j^{-1}$ translates the primitive cell at $\eta_j \tilde{\gamma}'$ to that at $\eta_i \tilde{\gamma}$. Our algorithms [39, 48] define hopping models on unit cells and extend models defined on a primitive cell to a supercell according to Eq. (4).

Reciprocal-space perspective.— In Euclidean lattices, translation symmetry constrains the form of Hamiltonian eigenstates via Bloch's theorem [49]. Similarly, the *automorphic Bloch theorem* for hyperbolic lattices [27] stipulates that eigenstates ψ_D of a translation-invariant Hamiltonian satisfy $\psi_D(\gamma^{-1}(z)) = D(\gamma)\psi_D(z)$, where $\gamma \in \Gamma$ is a translation, z the position coordinate, and D an IR of Γ . By contrast with Euclidean lattices, Γ has IRs of dimensions $d > 1$. Nevertheless, we can block-diagonalize [41] the Hamiltonian in Eq. (4) into blocks of Bloch Hamiltonians,

$$H(D) = \sum_{\tilde{\gamma} \in \Gamma^{(m)}} h(\tilde{\gamma}) \otimes D(\tilde{\gamma}), \quad (5)$$

where $h_{ij}^{uv}(\tilde{\gamma}) = h^{uv}(\eta_i \tilde{\gamma} \eta_j^{-1})$ is the hopping matrix within the supercell, and the unitary ($d \times d$)-matrix $D(\tilde{\gamma})$ generalizes the Bloch phase factor [14].

Generally, no parametrization of the IRs D is known, limiting a direct application of the automorphic Bloch theorem. However, the space of 1D IRs, the *Abelian BZ* (ABZ), is well-understood: if the cell is compactified on a manifold of genus

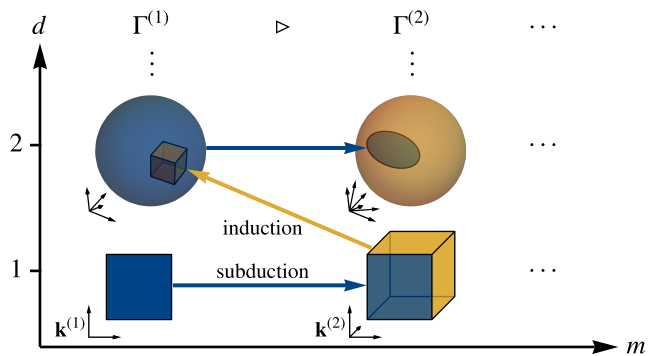


FIG. 3. Illustration of the spaces of d -dimensional irreducible representations (IRs) of a sequence of translation subgroups $\Gamma^{(m)}$ corresponding to supercells with $N^{(m)}$ primitive cells. The spaces of 1D IRs are hypertori (illustrated as square and cube) with dimension growing linearly with $N^{(m)}$, while the spaces of higher-dimensional IRs are more complicated (illustrated as balls). The IRs of $\Gamma^{(m)}$ of dimension d subduce (blue arrow) representations of $\Gamma^{(m+1)}$ of the same dimension and induce (yellow arrow) representations of $\Gamma^{(m-1)}$ of higher dimension (see text).

g, then ABZ is the $2g$ -dimensional torus T^{2g} parametrized by momenta $\{0 \leq k_i < 2\pi\}_{i=1}^{2g}$ and the IRs are defined on the $2g$ generators γ_i of Γ by $D_{\mathbf{k}}(\gamma_i) = e^{ik_i}$ [26–28]. While the ABZ sometimes is representative of the bulk spectrum of flakes [10–12, 23], important features can be missed [36, 37]. Studying the *non-Abelian* Bloch states is therefore crucial for a complete reciprocal-space description. Remarkably, as we explain below, AHBT applied to a sequence of supercells provides systematic access to non-Abelian Bloch states.

Considering the sequence of translation groups in Eq. (3), each $\Gamma^{(m)}$ has a tower of d -dimensional IRs with $d \geq 1$ (Fig. 3). However, due to the subgroup relationships, the IRs of different $\Gamma^{(m)}$ are *not* independent. First, the restriction of a d -dimensional IR of $\Gamma^{(m)}$ to its subgroup $\Gamma^{(m+1)}$ is a d -dimensional (possibly reducible) *subduced* representation of $\Gamma^{(m+1)}$. Second, any d -dimensional IR of $\Gamma^{(m)}$ implies a $(d|\Gamma^{(m-1)}/\Gamma^{(m)}|)$ -dimensional (possibly reducible) *induced* representation of $\Gamma^{(m-1)}$ [50]. Thus, 1D IRs of $\Gamma^{(m)}$ subduce 1D IRs of $\Gamma^{(m+1)}$, but because $\text{ABZ}^{(m+1)}$ has larger dimension than $\text{ABZ}^{(m)}$, there must be 1D IRs of $\Gamma^{(m+1)}$ that induce higher-dimensional IRs of $\Gamma^{(m)}$. Therefore, by studying the well-understood 1D IRs of supercells in the sequence, we gain access to a successively larger portion of higher-dimensional IRs of $\Gamma^{(1)}$. While this scheme does not reproduce *all* IRs, we conjecture that it converges to the thermodynamic limit [35] for $m \rightarrow \infty$.

Results.— We illustrate the supercell method by computing the DOS for selected hopping models on hyperbolic lattices: the previously studied octagon-kagome [11] and $\{8, 3\}$ -Haldane [10, 12] models, and a generalization to the $\{6, 4\}$ lattice of the Benalcazar-Bernevig-Hughes (BBH) model [51]. Each model is defined on a symmetric primitive cell and the DOS is computed [41] by randomly sampling $\text{ABZ}^{(m)}$ in a sequence satisfying Eq. (3). We observe rapid convergence with system size: Figs. 4a, 4b and 5b show data

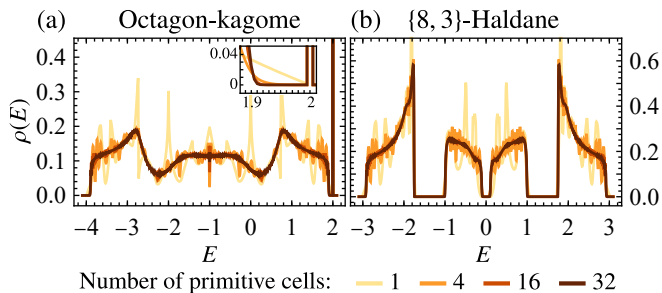


FIG. 4. Density of states ρ as a function of energy E of (a) the nearest-neighbor (NN) model on the octagon-kagome lattice and (b) the Haldane model on the $\{8, 3\}$ lattice with NN hopping $h_1 = 1$, next-NN hopping $h_2 = 1/6$, flux $\phi = \pi/2$, and sublattice mass $h_0 = 1/3$. The inset in (a) shows the depletion of $\rho(E)$ near the flat band at $E = 2$.

for systems with only up to 32 (768), 32 (512), and 64 (1536) primitive cells (sites), respectively. In sharp contrast, the DOS obtained from the corresponding PBC cluster (without applying AHBT) is extremely far from converged [41], demonstrating the computational power of our approach.

The NN hopping model on the octagon-kagome lattice has been analyzed in the context of flat bands in Ref. 11. Using real-space arguments, the authors describe a band touching between the flat band and the dispersive bands. In Fig. 4a, we observe that the DOS near the flat band is suppressed with increasing number of primitive cells N , suggesting that the gaplessness is a finite-size effect. This DOS suppression is consistent with the expected behavior near a band edge. Assuming a generic quadratic scaling of the energy dispersion with (Abelian) momentum near the band touching, $E \propto \mathbf{k}^2$, we obtain the DOS by integrating over the $2g$ -dimensional ABZ: $\rho(E) \sim \int d^{2g}\mathbf{k} \delta(E - v\mathbf{k}^2) \propto E^{g-1}$. Since g grows linearly with N [Eq. (1)], this explains the DOS suppression near band edges, indicated in Fig. 1f and observed in all models (Figs. 4 and 5b).

Next, we turn to the Haldane model on the $\{8, 3\}$ lattice [10, 12] which generalizes the original Haldane model on the honeycomb lattice [52]. We adopt the parameter choices of Ref. 10 and show the converging DOS in Fig. 4b. Crucially, the characteristic DOS suppression near the edges of all three gaps indicates that the gaps obtained from AHBT are stable to the inclusion of non-Abelian Bloch states and are not caused by finite-size effects.

Finally, motivated by the recent interest in higher-order topological phenomena on hyperbolic flakes [16, 17], we introduce the BBH model on the $\{6, 4\}$ lattice. Similar to its original version on the square lattice [51], the model is defined on a lattice with fourfold coordination, has four orbitals per site, and exhibits π -fluxes through the quadrilateral plaquettes (Fig. 5a). The intra-site hopping h_0 may differ from the inter-site hopping h_1 . As in the Euclidean case, this arrangement leads to a *trivial* phase for $|h_0| \gg |h_1|$ with effectively independent rings centered at lattice sites, and a *nontrivial* phase for $|h_0| \ll |h_1|$ with effectively independent rings centered on the plaquettes. The computed DOS for the two phases and the transition are shown in Fig. 5b. The trivial and the nontrivial phase both

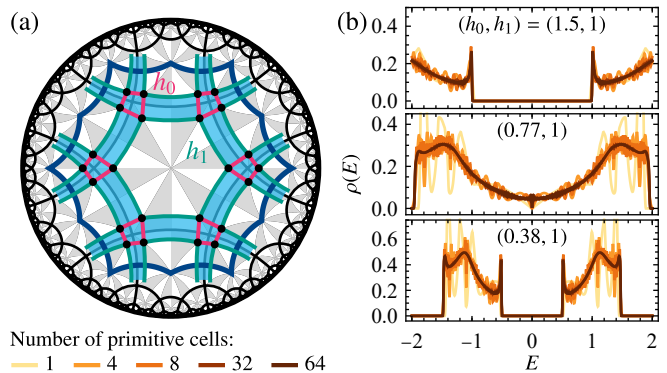


FIG. 5. Benalcazar-Bernevig-Hughes model on the $\{6, 4\}$ lattice. (a) Model definition on the primitive cell (blue polygon) of the $\{6, 4\}$ lattice (black lines). There are four orbitals (black dots) at each site, coupled by inter-site hoppings h_0 (magenta) and intra-site hoppings h_1 (green). Light blue shading of plaquettes bounded by magenta/green lines indicates π -fluxes. (b) Density of states for the indicated choices of (h_0, h_1) . The top/middle/bottom subpanel corresponds to the trivial/critical/nontrivial phase.

exhibit an energy gap that remains stable when going to larger supercells. The gap closes at $h_0/h_1 \approx 0.77$, indicating a phase transition. Interestingly, for small supercells the transition appears semimetallic with vanishing DOS at $E = 0$. However, this is a finite-size effect and the DOS ultimately converges to a finite value, implying a *metallic* transition.

Conclusions.— We have introduced a method for systematically studying non-Abelian Bloch states in hyperbolic lattices by applying Abelian hyperbolic band theory to sequences of supercells, in analogy to zone folding in solid-state physics. This provides a substantial step toward a complete reciprocal-space description, which we believe to be consistent with recent work [34, 35] in real space. While real-space methods scale suboptimally due to the increasing number of noncontractible loops [37], the combination of real-space supercells with reciprocal-space momenta in our approach appears to mitigate this problem and additionally provides true bulk states instead of finite-size approximations. Our DOS results on gapless elementary nearest-neighbor models are in agreement with previous results obtained using a different method [37], but we additionally studied topological models exhibiting energy gaps. Our method has three substantial advantages over Ref. 37: (i) it gives direct access to bulk eigenstates, (ii) it allows for parallel computation through separating the Hilbert space into \mathbf{k} -sectors, and (iii) there is no extra computational cost for longer-range hoppings.

Looking ahead, we anticipate our reciprocal-space supercell method will facilitate advances in HBT such as symmetry analysis [12], low-energy expansions [36], and topological band theory, including the recently studied 2D hyperbolic model [22] with nontrivial second Chern number [36]. Developing systematic algorithms for generating longer sequences of $\Delta/\Gamma^{(m)}$ quotients beyond those in Ref. 38 would be beneficial for achieving better convergence. Finally, we hope the implementation of our approach in a publicly available software package [39, 48, 53] will accelerate further studies of

hyperbolic quantum matter.

Acknowledgments.— We would like to thank I. Boettcher, A. Chen, A. Stegmaier, L. K. Upreti, S. Dey, T. Neupert, E. Prodan, and T. Tummuru for valuable discussions and R. Mosseri and J. Vidal for sharing their data, allowing a quantitative comparison of our results. P. M. L. and T. B. were supported by the Ambizione grant No. 185806 by the Swiss National Science Foundation (SNSF). P. M. L. is grateful for the hospitality of the Theoretical Physics Institute at the University of Alberta, where part of this work was completed. T. B. was supported by the Starting Grant No. 211310 by SNSF. J. M. was supported by NSERC Discovery Grants #RGPIN-2020-06999 and #RGPAS-2020-00064; the Canada Research Chair (CRC) Program; the Government of Alberta’s Major Innovation Fund (MIF); the Tri-Agency New Frontiers in Research Fund (NFRF, Exploration Stream); and the Pacific Institute for the Mathematical Sciences (PIMS) Collaborative Research Group program.

-
- [1] A. J. Kollár, M. Fitzpatrick, and A. A. Houck, Hyperbolic lattices in circuit quantum electrodynamics, *Nature* **571**, 45 (2019).
- [2] P. M. Lenggenhager, A. Stegmaier, L. K. Upreti, T. Hofmann, T. Helbig, A. Vollhardt, M. Greiter, C. H. Lee, S. Imhof, H. Brand, T. Kießling, I. Boettcher, T. Neupert, R. Thomale, and T. Bzdušek, Simulating hyperbolic space on a circuit board, *Nat. Commun.* **13**, 4373 (2022).
- [3] S. Yu, X. Piao, and N. Park, Topological hyperbolic lattices, *Phys. Rev. Lett.* **125**, 053901 (2020).
- [4] I. Boettcher, P. Bienias, R. Belyansky, A. J. Kollár, and A. V. Gorshkov, Quantum simulation of hyperbolic space with circuit quantum electrodynamics: From graphs to geometry, *Phys. Rev. A* **102**, 032208 (2020).
- [5] A. Saa, E. Miranda, and F. Rouxinol, Higher-dimensional Euclidean and non-Euclidean structures in planar circuit quantum electrodynamics, *arXiv:2108.08854* (2021).
- [6] X. Zhu, J. Guo, N. P. Breuckmann, H. Guo, and S. Feng, Quantum phase transitions of interacting bosons on hyperbolic lattices, *J. Phys.: Condens. Matter* **33**, 335602 (2021).
- [7] A. Stegmaier, L. K. Upreti, R. Thomale, and I. Boettcher, Universality of Hofstadter butterflies on hyperbolic lattices, *Phys. Rev. Lett.* **128**, 166402 (2022).
- [8] M. Ruzzene, E. Prodan, and C. Prodan, Dynamics of elastic hyperbolic lattices, *Extreme Mech. Lett.* **49**, 101491 (2021).
- [9] P. Bienias, I. Boettcher, R. Belyansky, A. J. Kollár, and A. V. Gorshkov, Circuit quantum electrodynamics in hyperbolic space: From photon bound states to frustrated spin models, *Phys. Rev. Lett.* **128**, 013601 (2022).
- [10] D. M. Urwyler, P. M. Lenggenhager, I. Boettcher, R. Thomale, T. Neupert, and T. Bzdušek, Hyperbolic topological band insulators, *Phys. Rev. Lett.* **129**, 246402 (2022).
- [11] T. Bzdušek and J. Maciejko, Flat bands and band-touching from real-space topology in hyperbolic lattices, *Phys. Rev. B* **106**, 155146 (2022).
- [12] A. Chen, Y. Guan, P. M. Lenggenhager, J. Maciejko, I. Boettcher, and T. Bzdušek, Symmetry and topology of hyperbolic haldane models, *Phys. Rev. B* **108**, 085114 (2023).
- [13] R. Mosseri, R. Vogeler, and J. Vidal, Aharonov-Bohm cages, flat bands, and gap labeling in hyperbolic tilings, *Phys. Rev. B* **106**, 155120 (2022).
- [14] N. Cheng, F. Serafin, J. McInerney, Z. Rocklin, K. Sun, and X. Mao, Band Theory and Boundary Modes of High-Dimensional Representations of Infinite Hyperbolic Lattices, *Phys. Rev. Lett.* **129**, 088002 (2022).
- [15] Z.-R. Liu, C.-B. Hua, T. Peng, and B. Zhou, Chern insulator in a hyperbolic lattice, *Phys. Rev. B* **105**, 245301 (2022).
- [16] Y.-L. Tao and Y. Xu, Higher-order topological hyperbolic lattices, *Phys. Rev. B* **107**, 184201 (2023).
- [17] Z.-R. Liu, C.-B. Hua, T. Peng, R. Chen, and B. Zhou, Higher-order topological insulators in hyperbolic lattices, *Phys. Rev. B* **107**, 125302 (2023).
- [18] P. Basteiro, G. D. Giulio, J. Erdmenger, J. Karl, R. Meyer, and Z.-Y. Xian, Towards explicit discrete holography: Aperiodic spin chains from hyperbolic tilings, *SciPost Phys.* **13**, 103 (2022).
- [19] P. Basteiro, R. N. Das, G. D. Giulio, and J. Erdmenger, Aperiodic spin chains at the boundary of hyperbolic tilings, *arXiv:2212.11292* (2022).
- [20] N. Gluscevich, A. Samanta, S. Manna, and B. Roy, Dynamic mass generation on two-dimensional electronic hyperbolic lattices, *arXiv:2302.04864* (2023).
- [21] W. Zhang, H. Yuan, N. Sun, H. Sun, and X. Zhang, Observation of novel topological states in hyperbolic lattices, *Nat. Commun.* **13**, 2937 (2022).
- [22] W. Zhang, F. Di, X. Zheng, H. Sun, and X. Zhang, Hyperbolic band topology with non-trivial second Chern numbers, *Nat. Commun.* **14**, 1083 (2023).
- [23] A. Chen, H. Brand, T. Helbig, T. Hofmann, S. Imhof, A. Fritzsche, T. Kießling, A. Stegmaier, L. K. Upreti, T. Neupert, T. Bzdušek, M. Greiter, R. Thomale, and I. Boettcher, Hyperbolic matter in electrical circuits with tunable complex phases, *Nat. Commun.* **14**, 622 (2023).
- [24] Q. Pei, H. Yuan, W. Zhang, and X. Zhang, Engineering boundary-dominated topological states in defective hyperbolic lattices, *Phys. Rev. B* **107**, 165145 (2023).
- [25] J. Chen, F. Chen, Y. Yang, L. Yang, Z. Chen, Y. Meng, B. Yan, X. Xi, Z. Zhu, G.-G. Liu, P. P. Shum, H. Chen, R.-G. Cai, R.-Q. Yang, Y. Yang, and Z. Gao, AdS/CFT Correspondence in Hyperbolic Lattices, *arXiv:2305.04862* (2023).
- [26] J. Maciejko and S. Rayan, Hyperbolic band theory, *Sci. Adv.* **7**, abe9170 (2021).
- [27] J. Maciejko and S. Rayan, Automorphic Bloch theorems for hyperbolic lattices, *Proc. Natl. Acad. Sci. U.S.A.* **119**, e2116869119 (2022).
- [28] I. Boettcher, A. V. Gorshkov, A. J. Kollár, J. Maciejko, S. Rayan, and R. Thomale, Crystallography of hyperbolic lattices, *Phys. Rev. B* **105**, 125118 (2022).
- [29] K. Ikeda, S. Aoki, and Y. Matsuki, Hyperbolic band theory under magnetic field and Dirac cones on a higher genus surface, *J. Phys.: Condens. Matter* **33**, 485602 (2021).
- [30] K. Ikeda, Y. Matsuki, and S. Aoki, Algebra of hyperbolic band theory under magnetic field, *arXiv:2107.10586* (2021).
- [31] E. Kienzle and S. Rayan, Hyperbolic band theory through Higgs bundles, *Adv. Math.* **409**, 108664 (2022).
- [32] Á. Nagy and S. Rayan, On the hyperbolic Bloch transform, *Ann. Henri Poincaré* [10.1007/s00023-023-01336-8](https://doi.org/10.1007/s00023-023-01336-8) (2023).
- [33] A. Attar and I. Boettcher, Selberg trace formula in hyperbolic band theory, *Phys. Rev. E* **106**, 034114 (2022).
- [34] F. R. Lux and E. Prodan, Spectral and combinatorial aspects of Cayley-crystals, *Annals of Henri Poincaré* [10.1007/s00023-023-01373-3](https://doi.org/10.1007/s00023-023-01373-3) (2023).
- [35] F. R. Lux and E. Prodan, Converging periodic boundary conditions and detection of topological gaps on regular hyperbolic tessellations, *Phys. Rev. Lett.* **131**, 176603 (2023).
- [36] T. Tummuru, A. Chen, P. M. Lenggenhager, T. Neupert, J. Ma-

- ciejko, and T. Bzdušek, Hyperbolic non-Abelian semimetal (2023), [arXiv:2307.09876](https://arxiv.org/abs/2307.09876).
- [37] R. Mosseri and J. Vidal, Density of states of tight-binding models in the hyperbolic plane, *Phys. Rev. B* **108**, 035154 (2023).
- [38] M. Conder, Quotients of triangle groups acting on surfaces of genus 2 to 101 (2007).
- [39] P. M. Lenggenhager, J. Maciejko, and T. Bzdušek, HyperCells: A GAP package for constructing primitive cells and supercells of hyperbolic lattices, <https://github.com/patrick-lenggenhager/HyperCells>, v0.9.0-beta: 10.5281/zenodo.10222599 (2023).
- [40] GAP, *GAP – Groups, Algorithms, and Programming, Version 4.11.1*, The GAP Group (2021).
- [41] See Supplemental Material, which cites additional Ref. 54–57, for further information on the definition of hopping models, the derivation of the Bloch Hamiltonian, the convergence of the supercell method, and on the models and data presented here.
- [42] N. W. Ashcroft and N. D. Mermin, *Solid State Physics* (Holt-Saunders, 1976).
- [43] F. Sausset and G. Tarjus, Periodic boundary conditions on the pseudosphere, *J. Phys. A: Math. Theor.* **40**, 12873 (2007).
- [44] R. Miranda, *Algebraic Curves and Riemann Surfaces* (American Mathematical Society, Providence, 1995).
- [45] W. Magnus, *Noneuclidean Tesselations and Their Groups* (Academic Press, New York, 1974).
- [46] C. J. Bradley and A. P. Cracknell, *The Mathematical Theory of Symmetry in Solids: Representation Theory for Point Groups and Space Groups* (Clarendon Press, Oxford, 1972).
- [47] W. Lück, Approximating L^2 -invariants by their finite-dimensional analogues, *Geom. Funct. Anal.* **4**, 455 (1994).
- [48] P. M. Lenggenhager, J. Maciejko, and T. Bzdušek, HyperBloch: A Mathematica package for hyperbolic tight-binding models and the supercell method, <https://github.com/patrick-lenggenhager/HyperBloch>, v0.9.0: 10.5281/zenodo.10222866 (2023).
- [49] F. Bloch, Über die Quantenmechanik der Elektronen in Kristallgittern, *Z. Phys.* **52**, 555 (1929).
- [50] W. Fulton and J. Harris, *Representation Theory* (Springer, New York, 1991).
- [51] W. A. Benalcazar, B. A. Bernevig, and T. L. Hughes, Quantized electric multipole insulators, *Science* **357**, 61 (2017).
- [52] F. D. M. Haldane, Model for a quantum Hall effect without Landau levels: Condensed-matter realization of the “parity anomaly”, *Phys. Rev. Lett.* **61**, 2015 (1988).
- [53] P. M. Lenggenhager, J. Maciejko, and T. Bzdušek, Supplementary data and code for: Non-abelian hyperbolic band theory from supercells (1.0.1), 10.5281/zenodo.10479221 (2023).
- [54] J. Cano and B. Bradlyn, Band Representations and Topological Quantum Chemistry, *Annu. Rev. Condens. Matter Phys.* **12**, 225 (2020).
- [55] A. E. Brouwer and W. H. Haemers, *Spectra of Graphs* (Springer, 2012).
- [56] D. J. S. Robinson, *A Course in the Theory of Groups*, 2nd ed. (Springer, New York, 1996).
- [57] T. Bzdušek and M. Sigrist, Robust doubly charged nodal lines and nodal surfaces in centrosymmetric systems, *Phys. Rev. B* **96**, 155105 (2017).

Supplemental Material for: Non-Abelian hyperbolic band theory from supercells

Patrick M. Lenggenhager ^{1,2,3,4,*} Joseph Maciejko ^{4,5,†} and Tomáš Bzdusek ^{1,2,‡}

¹Department of Physics, University of Zurich, Winterthurerstrasse 190, 8057 Zurich, Switzerland

²Condensed Matter Theory Group, Paul Scherrer Institute, 5232 Villigen PSI, Switzerland

³Institute for Theoretical Physics, ETH Zurich, 8093 Zurich, Switzerland

⁴Theoretical Physics Institute, University of Alberta, Edmonton, Alberta T6G 2E1, Canada

⁵Department of Physics, University of Alberta, Edmonton, Alberta T6G 2E1, Canada

(Dated: January 18, 2024)

CONTENTS

I. Hyperbolic tight-binding models	1
A. Algebraic labeling of Wyckoff positions and unit cells	2
1. Tiling by Schwarz triangles	2
2. Bravais lattice and unit cells	3
3. Supercells	4
B. Hopping Hamiltonian	5
C. Bloch Hamiltonian	6
II. Hopping models	8
A. Nearest-neighbor hopping models on $\{p, q\}$ lattices	9
1. $\{8, 8\}$ lattice	9
2. $\{8, 3\}$ lattice	11
3. Origin of the observed dips in the computed spectra at $E = 0$	12
B. Nearest-neighbor models on kagome lattices	13
C. Haldane model on $\{8, 3\}$ lattice	13
D. Benalcazar-Bernevig-Hughes model on $\{6, 4\}$ lattice	14
1. $\{6, 4\}$ lattice	14
2. Benalcazar-Bernevig-Hughes model	14
III. Convergence of the supercell method	15
A. Convergence with number of points in the Abelian Brillouin zone	15
B. Comparison of different supercell sequences	17
C. Comparison to continued-fraction method	17

I. HYPERBOLIC TIGHT-BINDING MODELS

Generically, a tight-binding model is defined in real space by orbitals at certain positions with nontrivial on-site symmetry group, so-called *Wyckoff positions*, and couplings between them. Thus, the first step in describing hyperbolic tight-binding models is to find and enumerate these Wyckoff positions. In Section **IA** we describe how to label the Wyckoff positions based on the triangle group, first in the infinite lattice, then on the lattice subdivided into unit cells, and finally on the lattice subdivided into supercells, which themselves are subdivided into primitive cells. Next, in Section **IB**, we discuss generic forms of hopping Hamiltonians defined on infinite lattices and on finite clusters with periodic boundary conditions (PBC). Finally, in Section **IC**, we show how to block-diagonalize the Hamiltonian in terms of blocks of generalized Bloch Hamiltonians.

* plengg@pks.mpg.de

† maciejko@ualberta.ca

‡ tomas.bzdusek@uzh.ch

A. Algebraic labeling of Wyckoff positions and unit cells

To define tight-binding models in real space, we first need to develop a systematic method for labeling the potential positions of orbitals, i.e., the lattice sites. These sites are typically located at high-symmetry positions, i.e., points with nontrivial on-site symmetry group, and depend on the underlying space group (the triangle group). Here, we limit our attention to the maximally symmetric positions, i.e., those whose site-symmetry groups are not a proper subgroup of any other site-symmetry group [54] (which for the regular $\{p, q\}$ tessellations correspond to centers of rotation symmetries), arriving at Eq. (S5).

Next, we discuss how to subdivide the infinite lattice into unit cells and identify a set of representatives of all high-symmetry positions contained within the unit cell; these are the (maximally symmetric) Wyckoff positions, cf. Eq. (S9). That allows us to relabel all sites in the infinite lattice in terms of the unit cell they are contained in and the corresponding Wyckoff position, cf. Eq. (S17).

Finally, we add two additional levels of subdivision: instead of covering the lattice directly with copies of a primitive cell, we subdivide it into large *super-supercells* composed of supercells, which themselves are composed of primitive cells. The motivation for doing this is that we may wish to consider large but finite PBC clusters instead of the infinite hyperbolic lattice. In this language, a finite PBC cluster can be described as a single super-supercell. In general, the primitive cells covering the infinite lattice are labeled according to Eq. (S20) in terms of which super-supercell, which supercell within the super-supercell, and which primitive cell within the supercell they lie in.

1. Tiling by Schwarz triangles

Recall from the main text that the triangle group

$$\Delta(r, q, p) = \langle a, b, c \mid a^2, b^2, c^2, (ab)^r, (bc)^q, (ca)^p \rangle \quad (\text{S1})$$

acts as a space group and tiles the plane by Schwarz triangles, cf. Fig. 2. By defining the right group action of Δ on the abstract set S of all Schwarz triangles, S can be viewed as generated by acting with all elements of Δ on one particular element of S , the fundamental Schwarz triangle (FST) s_f : $S = s_f \cdot \Delta$, cf. Fig. 2b.

The vertices of the Schwarz triangles in the tiling form a hyperbolic triangular lattice where each site has a nontrivial on-site symmetry group generated by the reflection symmetries with mirror lines passing through the vertex, cf. Fig. 2b. Here, we find it more convenient to work directly with the proper triangle group

$$\Delta^+(r, q, p) = \langle x, y, z \mid xyz, x^r, y^q, z^p \rangle, \quad (\text{S2})$$

with the embedding homomorphism $\Delta^+ \rightarrow \Delta$ defined by $x \mapsto ab, y \mapsto bc, z \mapsto ca$. The proper subgroup of the above-mentioned on-site symmetry group of a given vertex is then generated by the rotation around that vertex, cf. Fig. 2b. The set V of all vertices can be divided into three subsets V_z, V_y, V_x according to which vertex of the FST they originate from under action of Δ . Thus, we have $V = V_z \cup V_y \cup V_x$. Below we discuss V_z , but the discussion for the other two sets is analogous.

The on-site symmetry group of a vertex in V_z is

$$\Delta_z^+ = \langle z \mid z^p \rangle \quad (\text{S3})$$

and is exactly the stabilizer of that vertex if we define a right action of Δ^+ on the abstract set V_z . By the orbit-stabilizer theorem, there exists a bijection between the orbit $v_z \cdot \Delta^+$ of some $v_z \in V_z$ (assumed to be a vertex of the FST) and the quotient Δ^+/Δ_z^+ , or equivalently between V_z and the right transversal of Δ_z^+ in Δ^+

$$V_z \cong T_{\Delta^+}(\Delta_z^+). \quad (\text{S4})$$

Thus, the vertices are labelled by $(w, [t]_w)$ for $w \in \{x, y, z\}$ and $[t]_w \in \Delta^+/\Delta_w^+$ where a set of distinct cosets $[t]$ is given by a choice of representatives, i.e., the right transversal $T_{\Delta^+}(\Delta_w^+)$ mentioned above:

$$V \cong \{(w, [t]_w) : w \in \{x, y, z\}, t \in T_{\Delta^+}(\Delta_w^+)\}. \quad (\text{S5})$$

Note that for the orbit-stabilizer theorem it is important to pair right action with right cosets (and right transversal). Alternatively, we can work with the full groups Δ and Δ_z to arrive at the same conclusion: $V_z \cong T_{\Delta}(\Delta_z)$, because Δ is the semidirect product of Δ^+ with \mathbb{Z}_2 , the group generated by one of the reflections.

2. Bravais lattice and unit cells

The lattice formed by the vertices of the Schwarz triangles does not generally form a Bravais lattice. To obtain the Bravais lattice corresponding to a triangle group $\Delta(r, q, p)$, a translation group $\Gamma \triangleleft \Delta^+$ needs to be identified as discussed in the main text. The translation group then defines the subdivision of the infinite lattice into copies of the unit cell via the quotient group Δ/Γ (which is a group because $\Gamma \triangleleft \Delta$). Formally, we consider the decomposition of Δ into (disjoint) right cosets of Γ (which are equal to the left cosets, because $\Gamma \triangleleft \Delta$) using the transversal $T_\Delta(\Gamma)$:

$$\Delta = \bigcup_{g_j \in T_\Delta(\Gamma)} \Gamma g_j = \bigcup_{g_j \in T_\Delta(\Gamma)} g_j \Gamma = \bigcup_{\gamma \in \Gamma} T_\Delta(\Gamma) \gamma, \quad (\text{S6})$$

such that the set S of all Schwarz triangles is decomposed as

$$S = s_f \cdot \Delta = \bigcup_{\gamma \in \Gamma} s_f \cdot (T_\Delta(\Gamma) \gamma) = \bigcup_{\gamma \in \Gamma} (s_f \cdot T_\Delta(\Gamma)) \cdot \gamma, \quad (\text{S7})$$

i.e., S is divided into copies of $C = s_f \cdot T_\Delta(\Gamma)$ under action of the translation group:

$$S = \bigcup_{\gamma \in \Gamma} C \cdot \gamma = C \cdot \Gamma, \quad (\text{S8})$$

where C is interpreted as the set of Schwarz triangles in the unit cell. Above, we have emphasized the fact that $T_\Delta(\Gamma)$ is a set of chosen representatives of the cosets in Δ/Γ by labeling elements by g_j with the index j enumerating the representatives of different cosets. The choice of $T_\Delta(\Gamma)$ determines the unit cell in real space (relative to the FST), e.g., whether it is a connected region and whether it is symmetric under point-group operations. The software package [39] accompanying our work includes algorithms that choose $T_\Delta(\Gamma)$ such that C is connected and symmetric, given as input Δ^+/Γ and $w \in \{x, y, z\}$ specifying the center and therefore symmetry of the unit cell.

By the isomorphism theorem, the quotient Δ/Γ is isomorphic to the group G , which we interpret as the point group, since it maps the unit cell C to itself. Using this isomorphism, we can define the induced right action from G on C , such that $C = s_f \cdot G$. To label vertices, working with the proper subgroups is again more convenient (but not necessary). Note that the semidirect product structure of Δ implies $G^+ \cong \Delta^+/\Gamma$. Further, for any $w \in \{x, y, z\}$, Δ_w^+ , by definition in terms of a single rotation generator, does not have any torsion-free elements, such that the stabilizer G_w^+ of v_w (modulo translations in Γ) under the right action of G^+ is isomorphic to the full stabilizer: $G_w^+ \cong \Delta_w^+$. This now allows us to label the vertices in the unit cell, i.e., the Wyckoff positions: $V^C = V_z^C \cup V_y^C \cup V_x^C$ with $V_w^C \cong T_{G^+}(G_w^+)$, i.e.,

$$V^C \cong \{(w, [\delta]_w) : w \in \{x, y, z\}, \delta \in T_{G^+}(G_w^+)\}, \quad (\text{S9})$$

where $[\delta]_w \in G^+/G_w^+$. Note that the subscript again indicates the quotient group in which the coset lies. We now want to write *all* vertices, i.e., the infinite set V , in terms of translated Wyckoff positions, i.e., in terms of the finite set V^C and translations in Γ .

By the coset decomposition

$$\Delta^+ = \bigcup_{g_j \in T_{\Delta^+}(\Gamma)} g_j \Gamma, \quad (\text{S10})$$

any $t \in \Delta^+$ can be written as

$$t = g_j \gamma', \quad (\text{S11})$$

for unique $g_j \in T_{\Delta^+}(\Gamma)$ and $\gamma' \in \Gamma$. Using the quotient group isomorphism $i : \Delta^+/\Gamma \rightarrow G^+$, the image $i([g_j])$ of the unique coset $[g_j] \in \Delta^+/\Gamma$ associated with $g_j \in T_{\Delta^+}(\Gamma)$ can be rewritten using the right coset decomposition (for any choice of $w \in \{x, y, z\}$):

$$G^+ = \bigcup_{\delta_k \in T_{G^+}(G_w^+)} G_w^+ \delta_k, \quad (\text{S12})$$

i.e.,

$$i([g_j]) = i([w^n]) \delta_k \quad (\text{S13})$$

with unique $n \in \{0, 1, \dots, |G_w^+| - 1\}$ and $\delta_k \in T_{G^+}(G_w^+)$. Note that $n = n(j)$ and $k = k(j)$, i.e., they implicitly depend on the specific choice of j , but we suppress this dependence for better readability. Applying the inverse of i and recognizing that $i^{-1}(\delta_k) = [g]$ for a unique $g \in T_{\Delta^+}(\Gamma)$, which we denote by g_{u_w} to emphasize that $i([g_{u_w}]) \in T_{G^+}(G_w^+)$, results in

$$[g_j] = [w^n][g_{u_w}], \quad (\text{S14})$$

which in turn implies (due to $\Gamma \trianglelefteq \Delta^+$)

$$g_j = w^n g_{u_w} \gamma'', \quad (\text{S15})$$

for a unique $\gamma'' \in \Gamma$. Thus, we have shown that for any choice $w \in \{x, y, z\}$, an arbitrary $t \in \Delta^+$ can be written as

$$t = w^n g_{u_w} \gamma \quad (\text{S16})$$

for a unique $n \in \{0, 1, \dots, |G_w^+| - 1\}$, $g_{u_w} \in T_{\Delta^+}(\Gamma)$ with $i([g_{u_w}]) \in T_{G^+}(G_w^+)$, and $\gamma \in \Gamma$. Note that the order of the elements in Eq. (S16) is important (and is influenced by the fact that we use right action). The rotation w^n is to the very left, as required by the orbit-stabilizer theorem; when generating the set V by right action from the three vertices v_w , $w \in \{x, y, z\}$, w^n leaves v_w invariant due to being in its stabilizer Δ_w^+ . The order of g_{u_w} and γ , on the other hand, is physically motivated (mathematically, the opposite order would be equally valid, since $\Gamma \triangleleft \Delta^+$ implies that $g_{u_w} \gamma$ could be written with *different* translation to the left of g_{u_w} instead): g_{u_w} specifies the position of the vertex in each unit cell and then the *whole* unit cell containing all vertices is translated by γ .

This allows us to label all Wyckoff positions in the unit cell by $u = (w, [g_{u_w}]_w)$ where $[g_{u_w}]_w \in T_{G^+}(G_w^+)$. Correspondingly, Wyckoff positions in the infinite lattice can be labelled by (u, γ) , where $\gamma \in \Gamma$ labels the unit cell, i.e.,

$$V \cong \bigcup_{\gamma \in \Gamma} \{(u, \gamma) : u = (w, [g_{u_w}]_w), w \in \{x, y, z\}, g_{u_w} \in T_{\Delta^+}(\Gamma), i([g_{u_w}]) \in T_{G^+}(G_w^+)\}. \quad (\text{S17})$$

More practically, determining the set V of distinct vertices requires to first choose $T_{\Delta^+}(\Gamma) \subset \Delta^+$ and then find the subset of elements g_{u_w} satisfying $i([g_{u_w}]) \in T_{G^+}(G_w^+)$.

The software package [39] accompanying our work includes algorithms that, given G^+ and w as input, construct (1) a list of Wyckoff positions in the unit cell labelled by $u = (w, u_w)$, (2) the compactified nearest-neighbor graph formed by them, including corresponding translations γ for edges crossing the unit cell boundary, and (3) a minimal list of translation generators chosen from those to ensure that they are translations to adjacent unit cells.

Part of the output of those algorithms for two quotient groups of $\Delta(2, 8, 8)$ is illustrated in Fig. 2a. The set S of Schwarz triangles is shown as gray/white triangles, the subset $C^{(1)}$ corresponding to the primitive cell is indicated by the blue polygon and the subset $C^{(2)}$ corresponding to the first supercell by the orange polygon. The compactified nearest-neighbor graphs are not shown explicitly but can be inferred: edges go along sides of the Schwarz triangles and for a given cell (primitive or supercell) edges on the cell boundary are identified according to the translations that relate them. These translations can be either generators γ_i of the corresponding translation group (indicated by the corresponding index i), their inverses γ_i^{-1} (indicated by \bar{i}), or composite translations and their inverses. Specifically for the 2-supercell in Fig. 2a there are two pairs of boundary edges related by the composite translations: $\alpha = \tilde{\gamma}_5^{-1} \tilde{\gamma}_3^{-1} \tilde{\gamma}_1^{-1}$ and $\beta = \tilde{\gamma}_6^{-1} \tilde{\gamma}_4^{-1} \tilde{\gamma}_2^{-1}$.

3. Supercells

Above, we have introduced labels for Wyckoff positions and unit cells. Next, we consider supercells made up of primitive cells. We assume a normal sequence of translation groups $\Gamma^{(m)} \triangleleft \Delta^+$, $m \geq 1$, satisfying $\Gamma^{(m+1)} \triangleleft \Gamma^{(m)}$, as discussed in the main text. The primitive cells $C^{(1)}$ within the infinite lattice are labeled by $\gamma^{(1)} \in \Gamma^{(1)}$. Because $\Gamma^{(m)}$ is a normal subgroup of $\Gamma^{(1)}$, we can once more consider the coset decomposition

$$\Gamma^{(1)} = \bigcup_{\eta_i^{(1)} \in T_{\Gamma^{(1)}}(\Gamma^{(m)})} \eta_i^{(1)} \Gamma^{(m)}, \quad (\text{S18})$$

which implies that any $\gamma^{(1)} \in \Gamma^{(1)}$ can be decomposed into unique $\eta_i^{(1)} \in T_{\Gamma^{(1)}}(\Gamma^{(m)})$ and $\gamma^{(m)} \in \Gamma^{(m)}$:

$$\gamma^{(1)} = \eta_i^{(1)} \gamma^{(m)}, \quad (\text{S19})$$

where $\eta_i^{(1)} \in T_{\Gamma^{(1)}}(\Gamma^{(m)})$ now labels the primitive cells $C^{(1)}$ within a supercell $C^{(m)}$ and $\gamma^{(m)} \in \Gamma^{(m)}$ the supercells $C^{(m)}$ in the infinite lattice. Let us again comment on the order of group elements. The same argument as for the position of γ in Eq. (S16) applies here: $\eta_i^{(1)}$, which describes the internal structure of the supercell, appears to the left of the translation $\gamma^{(m)}$ connecting different copies of the supercell. With that order, if two primitive cells in some supercell are related by a translation generator $\eta_i^{(1)}$, the corresponding copies of the primitive cells in the translated supercell are still related by $\eta_i^{(1)}$.

We now consider a larger super-supercell $C^{(n)}$ given by $\Gamma^{(n)}$ with $n > m$. Such a super-supercell consists of copies of the smaller supercell $C^{(m)}$, which in turn consists of copies of the primitive cell $C^{(1)}$. Using the fact that for $\gamma^{(m)} \in \Gamma^{(m)}$ there exist

unique $\eta_{i'}^{(m)} \in T_{\Gamma^{(m)}}(\Gamma^{(n)})$ and $\gamma^{(n)} \in \Gamma^{(n)}$ such that $\gamma^{(m)} = \eta_{i'}^{(m)} \gamma^{(n)}$, we find that any $\gamma^{(1)} \in \Gamma^{(1)}$ can be decomposed into unique $\eta_i^{(1)} \in T_{\Gamma^{(1)}}(\Gamma^{(m)})$, $\eta_{i'}^{(m)} \in T_{\Gamma^{(m)}}(\Gamma^{(n)})$ and $\gamma^{(n)} \in \Gamma^{(n)}$:

$$\gamma^{(1)} = \eta_i^{(1)} \eta_{i'}^{(m)} \gamma^{(n)}. \quad (\text{S20})$$

We consistently label elements of $\Gamma^{(m)}$ with the corresponding superscript, e.g., $\gamma^{(m)} \in \Gamma^{(m)}$ and $\eta_{i'}^{(m)} \in \Gamma^{(m)}$, where the subscript indicates that $\eta_{i'}^{(m)}$ is an element of a transversal, in this case of $T_{\Gamma^{(m)}}(\Gamma^{(n)})$. Note that $\Gamma^{(m)} \subset \Gamma^{(1)}$, such that all elements in Eq. (S20) are elements of $\Gamma^{(1)}$.

B. Hopping Hamiltonian

In this subsection, we develop the formalism for defining hopping Hamiltonians on both infinite hyperbolic lattices as well as PBC clusters, based on the algebraic description of the lattice introduced in the previous subsection. We start by subdividing the infinite lattice into primitive cells, each of which contains orbitals at certain Wyckoff positions. This utilizes the decomposition given in Eqs. (S16) and (S17) and results in Eq. (S21). Next, we further subdivide the lattice into supercells $C^{(m)}$ consisting of several primitive cells. Based on the decomposition in Eq. (S19), this results in Eq. (S22). Finally, we add one more layer of subdivision: larger super-supercells $C^{(n)}$ consisting themselves of several copies of $C^{(m)}$. This last step reflects the decomposition in Eq. (S20) and results in Eq. (S24). Instead of working on the infinite lattice, one can consider finite PBC clusters: the PBC identify each site outside of the cluster with a particular site inside it. This allows us to immediately write down the Hamiltonians on PBC clusters formed by a *single* supercell $C^{(m)}$ or a single super-supercell $C^{(n)}$, in Eqs. (S23) and (S25), respectively.

A generic hopping Hamiltonian defined on the primitive cell $C^{(1)}$ with translation group $\Gamma^{(1)}$ and hopping amplitude $h^{uv}(\gamma)$ for hopping from orbital v in the unit cell to orbital u in the unit cell translated by γ is given by

$$\mathcal{H} = \sum_{\gamma^{(1)}, \check{\gamma}^{(1)} \in \Gamma^{(1)}} \sum_{u,v} h^{uv} \left(\gamma^{(1)} \check{\gamma}^{(1)-1} \right) c_{\gamma^{(1)}}^u \dagger c_{\check{\gamma}^{(1)}}^v, \quad (\text{S21})$$

where $c_{\check{\gamma}}^u \dagger$ is the creation operator for the orbital u in the unit cell $\check{\gamma}$. Note that the more generic amplitude $h^{uv}(\gamma^{(1)}, \check{\gamma}^{(1)})$ simplifies to $h^{uv}(\gamma^{(1)} \check{\gamma}^{(1)-1})$ due to translation invariance.

If we further subdivide the infinite lattice into supercells $C^{(m)}$ with translation group $\Gamma^{(m)}$, then the same Hamiltonian can be rewritten as

$$\mathcal{H} = \sum_{\gamma^{(m)}, \check{\gamma}^{(m)} \in \Gamma^{(m)}} \sum_{\eta_i^{(1)}, \eta_j^{(1)} \in T_{\Gamma^{(1)}}(\Gamma^{(m)})} \sum_{u,v} h^{uv} \left(\eta_i^{(1)} \gamma^{(m)} \check{\gamma}^{(m)-1} \eta_j^{(1)-1} \right) c_{\eta_i^{(1)} \gamma^{(m)}}^u \dagger c_{\eta_j^{(1)} \check{\gamma}^{(m)}}^v, \quad (\text{S22})$$

where we used the unique decomposition given in Eq. (S19). With simplified notation $\gamma^{(m)} \mapsto \check{\gamma}$, $\check{\gamma}^{(m)} \mapsto \check{\gamma}'$, and $\eta_i^{(1)} \mapsto \eta_i$, this is exactly the Hamiltonian appearing in Eq. (4). Restricting to a single copy of the supercell implies that sites related by some $\gamma^{(m)} \in \Gamma^{(m)}$ are identified. Formally, this is implemented by specifying the primitive cell not by elements of $\Gamma^{(1)}$, but by cosets $[\eta_i^{(1)}]_{(1,m)} \in \Gamma^{(1)}/\Gamma^{(m)}$, where $\eta_i^{(1)} \in T_{\Gamma^{(1)}}(\Gamma^{(m)})$. Here, we have introduced the subscript $(1, m)$ to indicate the type of coset. This results in the Hamiltonian for a finite PBC cluster:

$$\mathcal{H}_{m\text{-PBC}} = \sum_{\gamma^{(m)} \in \Gamma^{(m)}} \sum_{\eta_i^{(1)}, \eta_j^{(1)} \in T_{\Gamma^{(1)}}(\Gamma^{(m)})} \sum_{u,v} h^{uv} \left(\eta_i^{(1)} \gamma^{(m)} \eta_j^{(1)-1} \right) c_{[\eta_i^{(1)}]_{(1,m)}}^u \dagger c_{[\eta_j^{(1)}]_{(1,m)}}^v, \quad (\text{S23})$$

where we have set $\check{\gamma}^{(m)} = 1$, since we are now focusing on a single copy of the supercell $C^{(m)}$; however, we keep the summation over $\gamma^{(m)} \in \Gamma^{(m)}$ due to the possibility of long-range hopping processes in \mathcal{H} that exceed the size of a single supercell.

Next, we introduce another level of subdivision: an even larger super-supercell $C^{(n)}$ with $n > m$ consisting of copies of the supercell $C^{(m)}$. Using the unique decomposition given in Eq. (S20), we can rewrite Eq. (S22) as

$$\mathcal{H} = \sum_{\gamma^{(n)}, \check{\gamma}^{(n)} \in \Gamma^{(n)}} \sum_{\eta_{i'}^{(m)}, \eta_{j'}^{(m)} \in T_{\Gamma^{(m)}}(\Gamma^{(n)})} \sum_{\eta_i^{(1)}, \eta_j^{(1)} \in T_{\Gamma^{(1)}}(\Gamma^{(m)})} \sum_{u,v} h^{uv} \left(\eta_i^{(1)} \eta_{i'}^{(m)} \gamma^{(n)} \check{\gamma}^{(n)-1} \eta_{j'}^{(m)-1} \eta_j^{(1)-1} \right) c_{\eta_i^{(1)} \eta_{i'}^{(m)} \gamma^{(n)}}^u \dagger c_{\eta_j^{(1)} \eta_{j'}^{(m)} \check{\gamma}^{(n)}}^v, \quad (\text{S24})$$

which once more can be restricted to a PBC cluster, in this case to $C^{(n)}$:

$$\mathcal{H}_{n\text{-PBC}} = \sum_{\gamma^{(n)} \in \Gamma^{(n)}} \sum_{\eta_{i'}^{(m)}, \eta_{j'}^{(m)} \in T_{\Gamma^{(m)}}(\Gamma^{(n)})} \sum_{\eta_i^{(1)}, \eta_j^{(1)} \in T_{\Gamma^{(1)}}(\Gamma^{(m)})} \sum_{u,v} h^{uv} \left(\eta_i^{(1)} \eta_{i'}^{(m)} \gamma^{(n)} \eta_{j'}^{(m)-1} \eta_j^{(1)-1} \right) c_{[\eta_i^{(1)} \eta_{i'}^{(m)}]_{(1,n)}}^u \dagger c_{[\eta_j^{(1)} \eta_{j'}^{(m)}]_{(1,n)}}^v, \quad (\text{S25})$$

where primitive cells are now labeled by cosets $[\eta_j^{(1)} \eta_{j'}^{(m)}]_{(1,n)} \in \Gamma^{(1)}/\Gamma^{(n)}$ [note the difference with Eq. (S23)].

For simplicity, we temporarily suppress the internal structure of $C^{(m)}$ in terms of copies of $C^{(1)}$, introducing new orbital labels $\mu = (u, \eta_i^{(1)})$, $\nu = (v, \eta_j^{(1)})$ and creation/annihilation operators

$$c_{[\eta_{i'}^{(m)}]_{(m,n)}}^\mu = c_{[\eta_i^{(1)} \eta_{i'}^{(m)}]_{(1,n)}}^\mu \quad \text{and} \quad c_{[\eta_{j'}^{(m)}]_{(m,n)}}^\nu = c_{[\eta_j^{(1)} \eta_{j'}^{(m)}]_{(1,n)}}^\nu, \quad (\text{S26})$$

where $[\eta_{i'}^{(m)}]_{(m,n)} \in \Gamma^{(m)}/\Gamma^{(n)}$ now labels the copies of $C^{(m)}$, rather than copies of $C^{(1)}$ as did $[\eta_i^{(1)} \eta_{i'}^{(m)}]_{(1,n)}$, and μ takes care of copies of $C^{(1)}$ within $C^{(m)}$, such that still all copies of $C^{(1)}$ are captured. Then,

$$\mathcal{H}_{n\text{-PBC}} = \sum_{\gamma^{(n)} \in \Gamma^{(n)}} \sum_{\eta_{i'}^{(m)}, \eta_{j'}^{(m)} \in T_{\Gamma^{(m)}}(\Gamma^{(n)})} \sum_{\mu, \nu} h^{\mu\nu} \left(\eta_{i'}^{(m)} \gamma^{(n)} \eta_{j'}^{(m)-1} \right) c_{[\eta_{i'}^{(m)}]_{(m,n)}}^\mu \dagger c_{[\eta_{j'}^{(m)}]_{(m,n)}}^\nu, \quad (\text{S27})$$

where

$$h^{\mu\nu} \left(\eta_{i'}^{(m)} \gamma^{(n)} \eta_{j'}^{(m)-1} \right) = h^{uv} \left(\eta_i^{(1)} \eta_{i'}^{(m)} \gamma^{(n)} \eta_{j'}^{(m)-1} \eta_j^{(1)-1} \right) \quad (\text{S28})$$

forms the hopping matrix h defined on $C^{(m)}$.

C. Bloch Hamiltonian

In this subsection, we derive the Bloch Hamiltonian corresponding to the most general $\Gamma^{(1)}$ -translation-invariant hopping Hamiltonian. As discussed in the main text, the Bloch Hamiltonian depends on the choice of unit cell, i.e., the choice of translation subgroup that is considered. We assume a subdivision of the infinite lattice into supercells $C^{(m)}$ and ignore the additional internal translation-invariant structure of $C^{(m)}$ in terms of primitive cells, i.e., only $\Gamma^{(m)}$ is utilized. However, instead of doing that for the Hamiltonian defined on the infinite lattice [Eq. (S22)], we assume a finite but large PBC cluster made up of many copies of $C^{(m)}$. More precisely, we choose this finite PBC cluster to be a larger super-supercell $C^{(n)}$, i.e., we consider Eq. (S27). This reduces the full translation group $\Gamma^{(m)}$ to the quotient group $\Gamma^{(m)}/\Gamma^{(n)}$, such that we avoid dealing with the former infinite group. Below, we first show that the Hamiltonian given in Eq. (S27) can be block-diagonalized into blocks of Bloch Hamiltonians [Eqs. (S38) and (S39)].

Only at the end do we take the limit $n \rightarrow \infty$, thereby recovering the infinite lattice [34]. This corresponds to taking the limit of an infinitely large super-supercell $C^{(n)}$. In the main text, we have discussed the reciprocal space of the infinite lattice, which is the continuous space of irreducible representations (IRs) of the infinite group $\Gamma^{(m)}$. Alternatively, we could consider the discrete reciprocal space of a finite PBC cluster, i.e., the super-supercell $C^{(n)}$. This reciprocal space is spanned by the finitely many IRs of the *finite* group $\Gamma^{(m)}/\Gamma^{(n)}$ [27]. By the third isomorphism theorem [56], the sequence of normal subgroups $\Gamma^{(m+1)} \triangleleft \Gamma^{(m)}$ implies that, for fixed n , the quotients $\Gamma^{(m)}/\Gamma^{(n)}$ also form a sequence of normal subgroups:

$$\Gamma^{(m+1)}/\Gamma^{(n)} \triangleleft \Gamma^{(m)}/\Gamma^{(n)}. \quad (\text{S29})$$

Therefore, the subduction and induction of representations apply to that space as well. We anticipate that this provides an approximation of the thermodynamic limit [34] and converges to the full reciprocal space for $n \rightarrow \infty$.

Starting from Eq. (S27) we now derive the corresponding Bloch Hamiltonian implementing the translation symmetry due to the finite translation group $\Gamma^{(m)}/\Gamma^{(n)}$. Simplifying the notation, namely writing $\tilde{\gamma}$ for $\gamma^{(n)}$ and dropping the super- and subscripts of $\eta_i^{(m)}$ and of the cosets $[\cdot]_{(m,n)}$, respectively, the Hamiltonian on the finite $C^{(n)}$ PBC cluster reads

$$\mathcal{H}_{n\text{-PBC}} = \sum_{\tilde{\gamma} \in \Gamma^{(n)}} \sum_{\eta_i, \eta_j \in T_{\Gamma^{(m)}}(\Gamma^{(n)})} \sum_{\mu, \nu} h^{\mu\nu} \left(\eta_i \tilde{\gamma} \eta_j^{-1} \right) c_{[\eta_i]}^\mu \dagger c_{[\eta_j]}^\nu. \quad (\text{S30})$$

We recognize that $\eta_i \tilde{\gamma} = \gamma' \in \Gamma^{(m)}$ and by the coset decomposition of $\Gamma^{(m)}/\Gamma^{(n)}$ the sums over $\tilde{\gamma} \in \Gamma^{(n)}$ and $\eta_i \in T_{\Gamma^{(m)}}(\Gamma^{(n)})$ can be replaced by a sum over $\gamma' \in \Gamma^{(m)}$:

$$\mathcal{H}_{n\text{-PBC}} = \sum_{\gamma' \in \Gamma^{(m)}} \sum_{\eta_j \in T_{\Gamma^{(m)}}(\Gamma^{(n)})} \sum_{\mu, \nu} h^{\mu\nu} \left(\gamma' \eta_j^{-1} \right) c_{[\gamma']}^\mu \dagger c_{[\eta_j]}^\nu, \quad (\text{S31})$$

where in the subscript of the creation operator we used that η_i and $\gamma' = \eta_i \tilde{\gamma}$ are in the same coset of $\Gamma^{(m)}/\Gamma^{(n)}$. Next, for a given $\eta_j \in T_{\Gamma^{(m)}}(\Gamma^{(n)})$, γ' can be uniquely written as $\gamma \eta_j$ with $\gamma = \gamma' \eta_j^{-1} \in \Gamma^{(m)}$, allowing us to introduce the sum over $\gamma \in \Gamma^{(m)}$

instead:

$$\mathcal{H}_{n\text{-PBC}} = \sum_{\eta_j \in T_{\Gamma^{(1)}}(\Gamma^{(m)})} \sum_{\gamma \in \Gamma^{(m)}} \sum_{\mu, \nu} h^{\mu\nu}(\gamma) c_{[\gamma\eta_j]}^{\mu \dagger} c_{[\eta_j]}^{\nu}. \quad (\text{S32})$$

According to Eqs. (25-26) in Ref. 27,

$$c_{[\gamma\eta_j]}^{\mu \dagger} = \sum_i c_{[\eta_i]}^{\mu \dagger} \mathcal{U}_{ij}([\gamma]), \quad (\text{S33})$$

where the matrices

$$\mathcal{U}_{ij}([\gamma]) = \delta_{[\eta_i], [\gamma\eta_j]} \quad (\text{S34})$$

form the so-called *regular representation* of $\Gamma^{(m)}/\Gamma^{(n)}$ (note that in contrast to Ref. 27, we are using right cosets). The regular representation can be decomposed into a direct sum of all IRs, each appearing with multiplicity equal to their dimension d_λ [27], i.e., there exists a unitary transformation P such that

$$P\mathcal{U}([\gamma])P^{-1} = \bigoplus_{\lambda=1}^{\mathcal{N}} d_\lambda D^{(\lambda)}([\gamma]), \quad (\text{S35})$$

where \mathcal{N} is the number of conjugacy classes of $\Gamma^{(m)}/\Gamma^{(n)}$.

The above implies that $\mathcal{H}_{n\text{-PBC}}$ can be written in terms of those blocks:

$$\mathcal{H}_{n\text{-PBC}} = \sum_{\gamma \in \Gamma^{(m)}} \sum_{i,j} \sum_{\mu, \nu} h^{\mu\nu}(\gamma) c_{[\eta_i]}^{\mu \dagger} \mathcal{U}_{ij}([\gamma]) c_{[\eta_j]}^{\nu} \quad (\text{S36})$$

$$= \sum_{k,l} \sum_{\mu, \nu} \left(\sum_i P_{ki} c_{[\eta_i]}^{\mu} \right)^{\dagger} \sum_{\gamma \in \Gamma^{(m)}} h^{\mu\nu}(\gamma) \left(\bigoplus_{\lambda=1}^{\mathcal{N}} d_\lambda D^{(\lambda)}([\gamma]) \right)_{kl} \sum_j P_{lj} c_{[\eta_j]}^{\nu} \quad (\text{S37})$$

$$= \sum_{k,l} \sum_{\mu, \nu} \left(\sum_i P_{ki} c_{[\eta_i]}^{\mu} \right)^{\dagger} \left(\bigoplus_{\lambda=1}^{\mathcal{N}} d_\lambda \sum_{\gamma \in \Gamma^{(m)}} h(\gamma) \otimes D^{(\lambda)}([\gamma]) \right)_{kl}^{\mu\nu} \sum_j P_{lj} c_{[\eta_j]}^{\nu}, \quad (\text{S38})$$

where we recognize the Bloch Hamiltonian

$$H(D) = \sum_{\gamma \in \Gamma^{(m)}} h(\gamma) \otimes D([\gamma]) \quad (\text{S39})$$

with the hopping matrix $h(\gamma)$ on the supercell $C^{(m)}$ having components $h^{\mu\nu}(\gamma)$.

Recovering the subdivision into primitive cells using Eq. (S26), we have

$$\mathcal{H}_{n\text{-PBC}} = \sum_{k,l} \sum_{i,j} \sum_{u,v} \hat{c}_{i,k}^{\mu \dagger} \sum_{\gamma^{(m)} \in \Gamma^{(m)}} \underbrace{h^{uv}(\eta_i^{(1)} \gamma^{(m)} \eta_j^{(1)-1})}_{=: h_{ij}^{\mu\nu}(\gamma^{(m)})} \left(\bigoplus_{\lambda=1}^{\mathcal{N}} d_\lambda D^{(\lambda)} \left(\left[\gamma^{(m)} \right]_{(m,n)} \right) \right)_{kl} \hat{c}_{j,l}^{\nu} \quad (\text{S40})$$

$$= \sum_{k,l} \sum_{i,j} \sum_{u,v} \hat{c}_{i,k}^{\mu \dagger} \left(\bigoplus_{\lambda=1}^{\mathcal{N}} d_\lambda H(D^{(\lambda)}) \right)_{ijkl}^{\mu\nu} \hat{c}_{j,l}^{\nu} \quad (\text{S41})$$

with

$$\hat{c}_{i,k}^{\mu} = \sum_{i'} P_{ki'} c_{[\eta_i^{(1)} \eta_{i'}^{(m)}]}^{\mu} \Big|_{(1,n)}, \quad (\text{S42})$$

and the Bloch Hamiltonian $H(D)$ with matrix elements

$$H_{ijk^{(\lambda)l}^{(\lambda)}}^{\mu\nu}(D^{(\lambda)}) = \sum_{\gamma^{(m)} \in \Gamma^{(m)}} h_{ij}^{\mu\nu}(\gamma^{(m)}) D_{k^{(\lambda)l}^{(\lambda)}}^{(\lambda)} \left(\left[\gamma^{(m)} \right]_{(m,n)} \right). \quad (\text{S43})$$

To avoid confusion, let us at this point remind ourselves of the meaning of all the indices appearing in Eqs. (S41) to (S43). The superscript (m) labels the translation group $\Gamma^{(m)}$ of the supercell $C^{(m)}$ and the subscript (m, n) indicates that $[\gamma^{(m)}]_{(m, n)}$ denotes the coset $\gamma^{(m)}\Gamma^{(n)}$. The IRs $D^{(\lambda)}$ of the finite group $\Gamma^{(m)}/\Gamma^{(n)}$ are labeled by λ and they span the reciprocal space of the PBC clusters formed by the super-supercell $C^{(n)}$. For a specific IR $D^{(\lambda)}$ the matrix indices $k^{(\lambda)}, l^{(\lambda)}$ range over the dimensions of the IR (and never arise in the Euclidean Bloch Hamiltonian due to the fact that Euclidean translation groups only have 1D IRs). The subscripts i, j label the copies of the primitive cell $C^{(1)}$ in the supercell $C^{(m)}$ and therefore range from 1 to $|\Gamma^{(1)}/\Gamma^{(m)}|$, while u, v range over the sites in the primitive cell $C^{(1)}$ (and therefore do not arise if applying Bloch's theorem to a single primitive cell).

Finally, we take the limit $n \rightarrow \infty$, i.e., we let the super-supercell $C^{(n)}$ encompass the whole infinite lattice. Formally, this implies the replacement of $\Gamma^{(m)}/\Gamma^{(n)}$ by $\Gamma^{(m)}$, such that Eq. (S22) is block-diagonalized as

$$\mathcal{H} = \sum_{k,l} \sum_{i,j} \sum_{u,v} \hat{c}_{i,k}^u \dagger \sum_{\gamma^{(m)} \in \Gamma^{(m)}} h_{ij}^{uv}(\gamma^{(m)}) \left(\bigoplus_{\lambda} d_{\lambda} D^{(\lambda)} \right)_{kl} (\gamma^{(m)}) \hat{c}_{j,l}^v \quad (\text{S44})$$

$$= \sum_{k,l} \sum_{i,j} \sum_{u,v} \hat{c}_{i,k}^u \dagger \left(\bigoplus_{\lambda} d_{\lambda} H(D^{(\lambda)}) \right)_{ijkl}^{uv} \hat{c}_{j,l}^v \quad (\text{S45})$$

with Bloch Hamiltonian given in Eq. (5) of the main text,

$$H(D) = \sum_{\gamma^{(m)} \in \Gamma^{(m)}} h(\gamma^{(m)}) \otimes D(\gamma^{(m)}), \quad (\text{S46})$$

where D is now an IR of $\Gamma^{(m)}$, and

$$\hat{c}_{i,k}^u = \sum_{i'} P_{ki'} c_{\eta_i^{(1)} \eta_{i'}^{(m)}}^u. \quad (\text{S47})$$

Let us remark that in Eq. (S45), we have kept the symbol “ \oplus ”, even though in reality the direct sum now goes over a *continuous* space of infinitely many IRs and a suitable measure over the representation space needs to be introduced [32]. We leave the question of a mathematical formalization of the $n \rightarrow \infty$ limit for future studies.

In this work, we only ever *explicitly* sample the subspace of one-dimensional (1D) IRs, i.e., the Abelian Brillouin zone (ABZ), which for the supercell $C^{(m)}$ is given by

$$\text{ABZ}^{(m)} = \left\{ \gamma_i^{(m)} \mapsto D_{\mathbf{k}^{(m)}}(\gamma_i^{(m)}) = e^{i\mathbf{k}^{(m)} \cdot \mathbf{r}_i} : \mathbf{k}^{(m)} \in \mathbb{T}^{2g^{(m)}} \right\}, \quad (\text{S48})$$

with the generators $\gamma_i^{(m)}$ of $\Gamma^{(m)}$. The *Abelian Bloch Hamiltonian* is then given according to Eq. (S46):

$$H^{(m)}(\mathbf{k}^{(m)}) = \sum_{\gamma^{(m)} \in \Gamma^{(m)}} h(\gamma^{(m)}) e^{i \sum_{i=1}^{2g^{(m)}} K_i k_i}, \quad (\text{S49})$$

where $g^{(m)}$ is the genus of the compactified $C^{(m)}$ cell, and K_i the number of times the generator $\gamma_i^{(m)}$ appears in $\gamma^{(m)}$ minus the number of times its inverse appears.

II. HOPPING MODELS

In this section, we give additional details on the models discussed in the main text. We specifically:

- (i) provide explicit expressions for the Hamiltonians and for the quotient groups $\Delta/\Gamma^{(m)}$ specifying the supercells in Sections II A to II D,
- (ii) illustrate the primitive cells and the model definitions of the Hamiltonians in Fig. S1 and illustrate their supercells in Fig. S2,
- (iii) show their density of states (DOS) in more detail in Figs. S3 and S4, and give the necessary parameters required to reproduce the data, i.e., sampling parameters.

Note that in the supplementary data and code [53] we make available the graphs representing the triangular tessellations, the lattices, the model Hamiltonians, and the supercells produced with our software package [39, 48], as well as the DOS data. Furthermore, we provide example code on how to obtain and handle those objects.

A. Nearest-neighbor hopping models on $\{p, q\}$ lattices

We start with the nearest-neighbor (NN) hopping models on $\{p, q\}$ lattices, whose sites are given by only the elements of $V_y \cong T_{\Delta^+}(\Delta_y^+)$, i.e., the q -fold rotation-symmetric vertices of the Schwarz triangles of $\Delta(2, q, p)$. In the main text, we have only briefly discussed the $\{8, 8\}$ lattice, for which we have not shown all the data. Here, we show the full data in Section II A 1 and Fig. S3a. While the NN hopping model on the $\{8, 3\}$ lattice was not explicitly discussed in the main text, we briefly discuss it here because of its relation to the NN hopping model on the octagon-kagome lattice and to the $\{8, 3\}$ -Haldane model, which all share $\Delta(2, 3, 8)$ as their space group.

1. $\{8, 8\}$ lattice

The $\{8, 8\}$ lattice is defined by the hyperbolic tessellation where eight octagons meet at each vertex, cf. Fig. S1a. Its space group is the triangle group $\Delta(2, 8, 8)$ and the minimal unit cell, i.e., the primitive cell (depicted as a blue polygon in Fig. S1a) is given by the smallest quotient $T2.6$ of Δ by one of its normal subgroups $\Gamma^{(1)}$ [38]:

$$G = \langle a, b, c \mid a^2, b^2, c^2, (ab)^2, (bc)^8, (ca)^8, (abc)^2, (bc)^3(ca)^{-1} \rangle, \quad (\text{S50})$$

with the generators a, b, c the reflections across the sides of the Schwarz triangle, cf. Fig. 2. With G isomorphic to the quotient group $\Delta/\Gamma^{(1)}$, $\Gamma^{(1)}$ is given by the kernel of that isomorphism, which can be extracted using GAP. With our algorithm for constructing symmetric unit cells [39], we obtain

$$\Gamma^{(1)} = \langle \gamma_1, \gamma_2, \gamma_3, \gamma_4 \mid \gamma_2\gamma_1^{-1}\gamma_4^{-1}\gamma_3\gamma_2^{-1}\gamma_1\gamma_4\gamma_3^{-1} \rangle \quad (\text{S51})$$

$$= \langle \gamma_1, \gamma_2, \gamma_3, \gamma_4 \mid \gamma_1\gamma_2^{-1}\gamma_3\gamma_4^{-1}\gamma_1^{-1}\gamma_2\gamma_3^{-1}\gamma_4 \rangle \quad (\text{S52})$$

and recognize the translation group of the Bolza cell which has been discussed extensively in recent literature [10, 12, 26, 27] on hyperbolic tight-binding models, since it is the maximal translation group of the $\{8, 8\}$, $\{8, 3\}$, and $\{8, 4\}$ lattices [28].

Using GAP, we have found a normal sequence of translation subgroups $\Gamma^{(m)} \triangleleft \Delta(2, 8, 8)$ via the appropriate quotient groups $G^{(m)} \cong \Delta/\Gamma^{(m)}$ given in Ref. 38, whose supercells preserve a maximum amount of symmetry. Using

$$x = ab, \quad y = bc, \quad z = ca, \quad (\text{S53})$$

the quotient groups have the following presentations:

$$\begin{aligned} G^{(1)} = G^{T2.6} &= \langle a, b, c \mid a^2, b^2, c^2, x^2, y^8, z^8, xzy, y^3z^{-1} \rangle, \\ G^{(2)} = G^{T3.11} &= \langle a, b, c \mid a^2, b^2, c^2, x^2, y^8, z^8, xzy \rangle, \\ G^{(3)} = G^{T5.13} &= \langle a, b, c \mid a^2, b^2, c^2, x^2, y^8, z^8, xy^{-2}z^{-1}y, xzy^{-1}z^{-2} \rangle, \\ G^{(4)} = G^{T9.20} &= \langle a, b, c \mid a^2, b^2, c^2, x^2, y^8, z^8, xy^{-2}z^{-1}y \rangle, \\ G^{(5)} = G^{T17.29} &= \langle a, b, c \mid a^2, b^2, c^2, x^2, y^8, z^8, xzy^{-2}z^{-2}y, (yz^{-1}y^2)^2 \rangle, \\ G^{(6)} = G^{T33.44} &= \langle a, b, c \mid a^2, b^2, c^2, x^2, y^8, z^8, xzy^{-2}z^{-2}y \rangle, \\ G^{(7)} = G^{T65.78} &= \langle a, b, c \mid a^2, b^2, c^2, x^2, y^8, z^8, xy^{-1}zy^{-2}(z^{-1}y)^2, x(zzy^{-1})^2z^{-2}yz^{-1}, yxz^2y^2xzy^{-1}z^{-1} \rangle. \end{aligned} \quad (\text{S54})$$

The corresponding connected symmetric supercells are illustrated in Fig. S2a and their triangle group graphs as well as boundary identifications are given in the supplementary data and code [53]. Note that by construction they all preserve the symmetries that leave their center invariant, i.e., eight-fold rotation and mirrors through the center.

Each octagon of the $\{8, 8\}$ tessellation corresponds to a copy of the primitive unit cell and there is a single site in its center shown as a black dot in Fig. S1a. The NN model on the $\{8, 8\}$ lattice thus has the Hamiltonian

$$\mathcal{H} = - \sum_{\langle i, j \rangle} c_i^\dagger c_j, \quad (\text{S55})$$

where $\langle i, j \rangle$ denotes the centers of two neighboring octagons. The hopping processes starting in the primitive unit cell are illustrated as red lines in Fig. S1a and the real-space hopping Hamiltonian is given in graph form in the supplementary data and code [53].

For each cell $C^{(m)}$ in the sequence given by Eq. (S54), we diagonalized the Abelian Bloch Hamiltonian $H^{(m)}(\mathbf{k}^{(m)})$ [given in Eq. (S49)] for 10^9 randomly sampled points in $T2^{\text{q}}(m)$ [corresponding to the ABZ given in Eq. (S48)]. From the eigenenergies

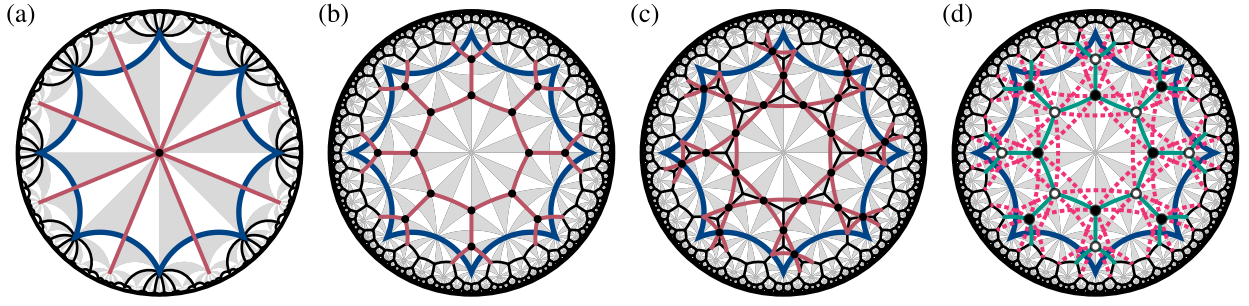


FIG. S1. Model definitions: primitive cells (blue polygon) with sites (black dots) and hoppings (red lines) for (a) the nearest-neighbor (NN) model on the $\{8, 8\}$ lattice, (b) the NN model on the $\{8, 3\}$ lattice, (c) the NN model on the octagon-kagome lattice (the line graph of the $\{8, 3\}$ lattice), and (d) the Haldane model on the $\{8, 3\}$ lattice. (d) The sublattice potential $\pm h_0$ is indicated by filled and empty disks on the sites, the NN hoppings h_1 are shown by green solid lines and the next-NN hoppings with amplitudes $h_2 e^{\pm i\phi}$ by dashed magenta lines.

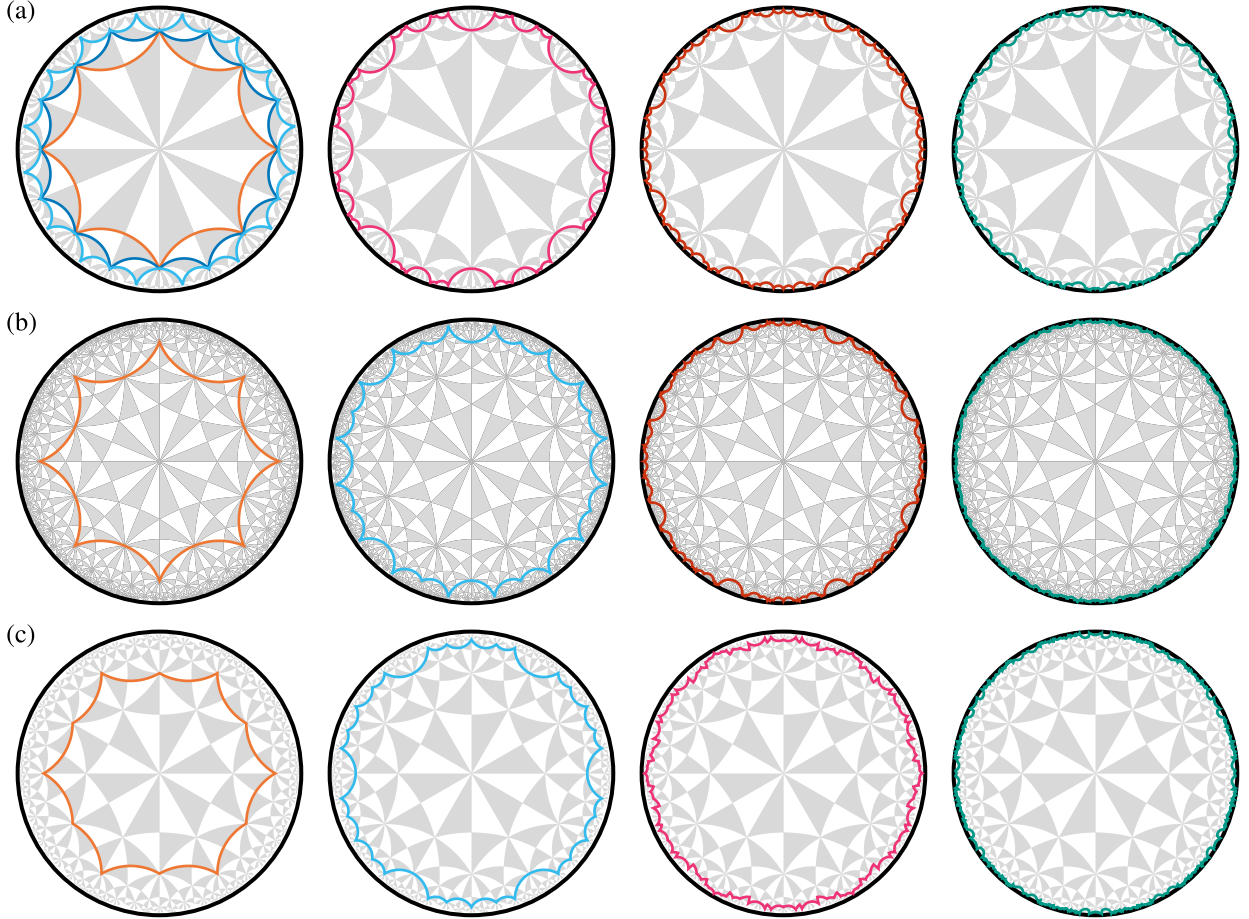


FIG. S2. Supercell sequences used to compute the density of states shown in the main text and in Figs. S3 and S4. The supercells are specified by the corresponding quotients $G \cong \Delta/\Gamma$ in the form “ Tg,j ”, denoting the j^{th} quotient of any triangle group $\Delta(r, q, p)$ having genus g [38]. Note that all the sequences start with a genus-2 unit cell, such that, per the Riemann-Hurwitz formula, $N = g - 1$ is the number of unit cells in the supercell. (a) $\Delta(2, 8, 8)$, relevant for the $\{8, 8\}$ lattice: T2.6, T3.11, T5.13, T9.20, T17.29, T33.44, [T65.78 (not shown)]. (b) $\Delta(2, 3, 8)$, relevant for the $\{8, 3\}$ lattice and the octagon-kagome lattice: T2.1, T5.1, T17.2, T33.1. (Note that the first two of the constructed super-cells match precisely those found for translation groups T2.6 and T5.13 for the $\Delta(2, 8, 8)$ lattice.) (c) $\Delta(2, 4, 6)$, relevant for the $\{6, 4\}$ lattice: T2.2, T5.4, T9.3, T33.11, [T65.9 (not shown)].

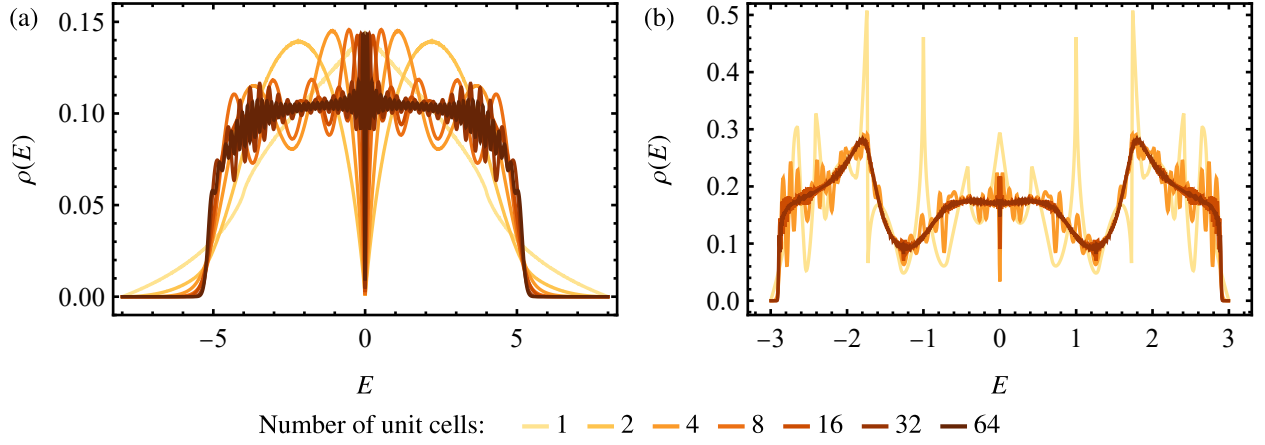


FIG. S3. Density of states of the nearest-neighbor hopping model on (a) the $\{8, 8\}$ and (b) the $\{8, 3\}$ lattice obtained using the supercell method. In (a) the supercell sequence T2.6, T3.11, T5.13, T9.20, T17.29, T33.44, T65.78 with 1, 2, 4, 8, 16, 32, 64 unit cells per supercell was used, while in (b) the sequence T2.1, T5.1, T17.2, T33.1 with 1, 4, 16, 32 unit cells was used. In both cases, the energy resolution is 0.005 with a moving average with window 0.01.

thus obtained, we computed the DOS $\rho^{(m)}(E)$ for an energy resolution of $dE = 0.005$, which was then smoothed using a moving average with window $2 dE = 0.01$, cf. Fig. S3a. In Fig. 1f in the main text we additionally show the additional red curve, which was obtained by extrapolating the data in Fig. S3a by eye, observing the fact that the DOS near the band edges becomes sharper, while the oscillations on the plateau are becoming smaller for larger supercells. We provide the raw data for the DOS in the supplementary data and code [53].

2. $\{8, 3\}$ lattice

The $\{8, 3\}$ lattice is defined by the hyperbolic tessellation where three octagons meet at each vertex, cf. Fig. S1b, and can therefore be considered a generalization of the honeycomb lattice [10]. Its space group is the triangle group $\Delta(2, 3, 8)$ and the primitive cell (blue polygon in Fig. S1b) is given by the quotient group $\Delta/\Gamma^{(1)}$ denoted by T2.1 [38]:

$$G = \langle a, b, c \mid a^2, b^2, c^2, (ab)^2, (bc)^3, (ca)^8, c(abc)^2 a(abc)^{-1} c^{-1} abca \rangle, \quad (\text{S56})$$

resulting in the translation group

$$\Gamma^{(1)} = \langle \gamma_1, \gamma_2, \gamma_3, \gamma_4 \mid \gamma_4 \gamma_1 \gamma_2^{-1} \gamma_3 \gamma_4^{-1} \gamma_1^{-1} \gamma_2 \gamma_3^{-1} \rangle \quad (\text{S57})$$

$$= \langle \gamma_1, \gamma_2, \gamma_3, \gamma_4 \mid \gamma_1 \gamma_2^{-1} \gamma_3 \gamma_4^{-1} \gamma_1^{-1} \gamma_2 \gamma_3^{-1} \gamma_4 \rangle, \quad (\text{S58})$$

which we once more identify as the translation group of the Bolza cell.

Using GAP, we have found a normal sequence of translation subgroups $\Gamma^{(m)} \triangleleft \Delta(2, 3, 8)$ via the appropriate quotient groups $G^{(m)} \cong \Delta/\Gamma^{(m)}$ given in Ref. 38: With x, y , and z given in Eq. (S53),

$$\begin{aligned} G^{(1)} &= G^{\text{T2.1}} = \langle a, b, c \mid a^2, b^2, c^2, x^2, y^3, z^8, zyxz(zx)^{-1}xz \rangle, \\ G^{(2)} &= G^{\text{T5.1}} = \langle a, b, c \mid a^2, b^2, c^2, x^2, y^3, z^8, z^3yz^{-1}xzy^{-1}xy^{-1}z^{-2}x \rangle, \\ G^{(3)} &= G^{\text{T17.2}} = \langle a, b, c \mid a^2, b^2, c^2, x^2, y^3, z^8, (z^2yx)^2(zx^{-1}z^{-1}x)^2 \rangle, \\ G^{(4)} &= G^{\text{T33.1}} = \langle a, b, c \mid a^2, b^2, c^2, x^2, y^3, z^8, xz^2(zyx)^3z^2y^2z^{-2}xy^{-1}z^{-2} \rangle, \end{aligned} \quad (\text{S59})$$

with the corresponding connected and symmetric supercells illustrated in Fig. S2b and their triangle group graphs as well as boundary identifications given in the supplementary data and code [53].

The $\{8, 3\}$ lattice is formed by all the three-fold symmetric points and the NN model has the Hamiltonian

$$\mathcal{H} = - \sum_{\langle i, j \rangle} c_i^\dagger c_j, \quad (\text{S60})$$

where $\langle i, j \rangle$ denotes the hopping along a side of an octagon, cf. Fig. S1b. The real-space hopping Hamiltonian is given in graph form in the supplementary data and code [53]. Again we consider the ABZ and Bloch Hamiltonian given in Eqs. (S48) and (S49),

respectively, but now for the sequence of supercells given in Eq. (S59). We randomly sampled 10^8 points in $\mathbb{T}^{2g^{(m)}}$, computed the spectrum of $H^{(m)}(\mathbf{k}^{(m)})$ and from that the DOS $\rho^{(m)}(E)$ for an energy resolution of $dE = 0.005$, which was then smoothed using a moving average with window $2dE = 0.01$, cf. Fig. S3b. We provide the raw data for the DOS in the supplementary data and code [53].

3. Origin of the observed dips in the computed spectra at $E = 0$

One systematic feature appearing in the presented DOS curves for the elementary NN model on both the $\{8, 3\}$ and the $\{8, 8\}$ lattice is the sharp dip at $E = 0$. This feature becomes narrower for computations on larger supercells, and is expected to vanish altogether when extrapolating to the thermodynamic limit. Below, we trace the appearance of this undesired behavior back to a chiral symmetry of these particular Hamiltonians, and explain how this feature is removed when enlarging the supercell. For concreteness, we explicitly consider the $\{8, 8\}$ model although the presented arguments can be adapted for any NN model on a bipartite lattice.

The elementary nearest-neighbor model on the $\{8, 8\}$ lattice has a single orbital per primitive cell, such that the Abelian Bloch states on that primitive cell form a single continuous band:

$$E(\mathbf{k}) = -2 \sum_{i=1}^4 \cos(k_i), \quad (\text{S61})$$

in the 4D Abelian Brillouin zone (BZ). The condition $E = 0$ implies that the states at zero energy form a (Fermi) surface with codimension 1 (i.e., a 3D hypersurface), resulting in a finite DOS at $E = 0$.

When considering a supercell, e.g., the 2-supercell, two things happen. First, the 4D BZ is reduced and the bands are folded, resulting in two bands in the reduced BZ. The specifics of this particular BZ reduction induced by extending the primitive cell to the 2-supercell are discussed in the Supplementary Material of Ref. 36. The two obtained bands trivially intersect at $E = 0$; yet, the computed DOS is unaffected by this step, because the band folding does not alter the collection of the captured eigenstates. In particular, the two bands are not coupled in the reduced BZ. This is because states in both bands still respect the full periodicity in primitive cells and carry a different value of a quantum number, namely of the initial four-component momentum.

Second, and this is the special feature of hyperbolic lattices, two more momentum components are introduced, increasing the BZ dimension from 4 to 6. Crucially, the two folded bands constructed on the reduced BZ are coupled when extended in these two additional momentum directions. Such a coupling is allowed because the states on the extended bands are no longer periodic in the primitive cells and thus no longer distinguished by the initial four-component momentum. As a result, the ensuing hybridization of the folded bands in the additional momentum directions transforms the trivial band crossings into band *nodes*.

To understand the codimension of the resulting nodes, one can rely on the existing literature on characterizing band nodes in various symmetry classes. Here, we apply the results and the terminology of Ref. 57, which points out the key role of ‘local-in- \mathbf{k} symmetries’, i.e., those that act on Bloch Hamiltonians while leaving momentum invariant. The codimension, in turn, explains the scaling of the DOS near $E = 0$.

In particular, the considered hyperbolic lattice model clearly has spinless time-reversal symmetry $\mathcal{T}^2 = +1$ which acts through complex conjugation and maps $\mathcal{T} : \mathbf{k} \mapsto -\mathbf{k}$. This symmetry can potentially be combined into a local-in- \mathbf{k} symmetry with a suitable inversion symmetry that also flips the sign of the momentum vector. In the 2-supercell of the $\{8, 8\}$ lattice, there are several inequivalent choices for the inversion center, namely a site, the mid-point of an edge, and the center of a face. It is derived in the Supplemental Material of Ref. 36, specifically around Eq. (F10), that it is the inversion with respect to the edge, \mathcal{P}_E , that acts on the supercell Bloch Hamiltonian by flipping the momentum sign: $\mathcal{P}_E : \mathbf{k} \mapsto -\mathbf{k}$. The composition $\mathcal{P}_E \mathcal{T}$ is therefore an antiunitary local-in- \mathbf{k} symmetry with $(\mathcal{P}_E \mathcal{T})^2 = +1$. Additionally, the Bloch Hamiltonian exhibits a sublattice symmetry \mathcal{S} because the two sites per 2-supercell form a bipartition of the lattice. Since the two sublattices are exchanged under inversion \mathcal{P}_E , the sublattice parity is odd [57] so that the local-in- \mathbf{k} particle-hole symmetry squares to $(\mathcal{S} \mathcal{P}_E \mathcal{T})^2 = -1$. The identified local-in- \mathbf{k} symmetries

$$\mathcal{S}, \quad (\mathcal{P}_E \mathcal{T})^2 = +1, \quad (\mathcal{S} \mathcal{P}_E \mathcal{T})^2 = -1 \quad (\text{S62})$$

locate the supercell Hamiltonian in nodal class CI, which exhibits band nodes of codimension $\delta = 2$ [57]. An analogous set of local-in- \mathbf{k} symmetries can also be identified in all the larger supercells. Importantly, the sublattice symmetry \mathcal{S} enforces a particle-hole symmetry of the spectrum at each \mathbf{k} . This pins all the nodes to the same energy $E = 0$, resulting in the pronounced dip in the computed DOS data.

Let us next discuss the character of this DOS suppression. Elementary integration can be used to show that band nodes of codimension δ pinned to $E = 0$ (and with the generically assumed linear dispersion) lead to the DOS scaling $\rho(E) \propto |E|^{\delta-1}$ [36]. In the considered model on the $\{8, 8\}$ lattice, $\delta = 2$ implies vanishing DOS at $E = 0$ with linear scaling. This is consistent with the dip of the 2-supercell data in Fig. 1f, and with the dips observed for larger supercells in Fig. S3 above.

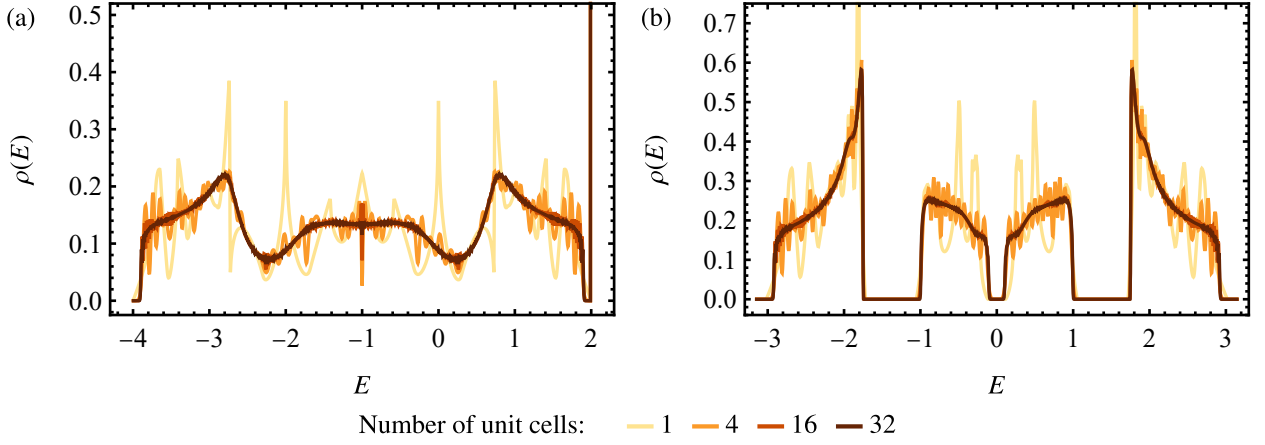


FIG. S4. Density of states of (a) the nearest-neighbor hopping model on the octagon-kagome lattice and (b) the Haldane model on the $\{8, 3\}$ lattice with $t_1 = 1$, $t_2 = 1/6$, $\phi = \pi/2$, $m = 1/3$ obtained using the supercell method. In both cases, data on the supercell sequence T2.1, T5.1, T17.2, T33.1 with 1, 4, 16, 32 unit cells is shown and the energy resolution is 0.005 with a moving average with window 0.01.

To understand how the dip ultimately disappears in the converged DOS for large supercells, first note that the band folding at each step multiplies the number of energy bands while keeping the overall bandwidth W fixed. Therefore, the energy extent ΔW of any individual band is expected to shrink with the size N of the N -supercell as $\Delta W \simeq W/N$. (If there are $M > 1$ sites per primitive cell, as is the case with $M = 16$ for the $\{8, 3\}$ lattice, then $\Delta W \simeq W/MN$.) At the same time, the linear DOS scaling $\rho(E) \propto |E|$ is an approximation that applies only in an energy range where the dispersion around the node can be linearly approximated. Since such a linear approximation cannot go beyond the energy extent of the band forming the node, the linear dip in the DOS is restricted to energies $|E| \lesssim W/MN$. This inequality explains the rapid shrinking of the dip at $E = 0$ with the growing supercell size N , visible in Fig. S3a, and also why the dip is significantly narrower in the $\{8, 3\}$ data in Fig. S3b.

We finally remark that the discussed dip is generically absent in models without sublattice/chiral symmetry. Since band nodes of such more general models are not pinned to a single value of energy, the node-induced DOS suppression is effectively smeared over a broader range of energies, resulting in smoother computed data.

B. Nearest-neighbor models on kagome lattices

The triangle group $\Delta(2, 3, p)$ allows not only constructing the $\{p, 3\}$ lattice, but also its line graph, the p -gon-kagome lattice with sites given by $V_x \cong T_{\Delta^+}(\Delta_x^+)$, i.e., the Schwarz triangle vertices with two-fold rotation symmetry. Here, we consider the octagon-kagome lattice, i.e., the case $p = 8$, cf. Fig. S1c. In the supplementary data and code [53], we additionally provide the real-space hopping Hamiltonian in graph form as well as the raw data for the DOS.

As an example, we study the octagon-kagome lattice, i.e., the line graph of the $\{8, 3\}$ lattice discussed above. The supercells and the corresponding translation groups do not depend on the internal structure of the primitive cells, i.e., where orbitals are placed. Thus, the discussion from the previous subsection applies to the octagon-kagome lattice and we can directly proceed to the results. Figures 4a and S4a show the DOS $\rho^{(m)}(E)$ obtained from randomly sampling 10^8 points in $T^{2g(m)}$ for an energy resolution of $dE = 0.005$ and smoothed using a moving average with window $2dE = 0.01$ for the sequence in Eq. (S59). Comparing Figs. S3b and S4a, we observe that the DOS of the NN model on the $\{8, 3\}$ lattice and on its line graph match up to the flat band at $E = 2$ in the latter case. This is consistent with what is expected from graph theory [55].

C. Haldane model on $\{8, 3\}$ lattice

The Haldane model on hyperbolic lattices has been introduced in Refs. 10, 12, and 21. The Hamiltonian illustrated in Fig. S1d takes the form [12]

$$\mathcal{H} = h_1 \sum_{\langle i, j \rangle} (c_i^\dagger c_j + \text{h.c.}) + h_2 \sum_{\overleftarrow{ij}} (e^{i\phi} c_i^\dagger c_j + \text{h.c.}) + h_0 \left(\sum_{i \in A} c_i^\dagger c_i - \sum_{i \in B} c_i^\dagger c_i \right) \quad (\text{S63})$$

with NN hopping amplitude h_1 (solid green lines), next-NN hopping amplitude $h_2 e^{i\phi}$ (dashed magenta lines), where \overleftarrow{ij} denotes hopping from site j to i in mathematically positive direction (counterclockwise) for a given octagon and ϕ is the flux parameter. Additionally, there is a staggered sublattice potential (called sublattice mass in the main text) $\pm h_0$ on the two sublattices A and B (filled and empty sites in the figure). In the supplementary data and code [53], we provide the real-space hopping Hamiltonian in graph form. We have chosen the same parameter values as Ref. 10: $h_1 = 1$, $h_2 = 1/6$, $\phi = \pi/2$, and $h_0 = 1/3$.

Given that the model is defined on the $\{8, 3\}$ lattice, the supercells are once more the ones given in Eq. (S59). In particular, the unit cell T2.1 is exactly the primitive cell used in Ref. 10, such that the DOS obtained from it matches the data presented there. With random sampling of 10^8 points in $\mathbb{T}^{2g(m)}$, we have computed the DOS with an energy resolution of $dE = 0.005$ and smoothed using a moving average with window $2 dE = 0.01$. The resulting data is shown in Figs. 4b and S4b and given as raw data in the supplementary data and code [53]. We observe the stability of all three energy gaps as we approach the thermodynamic limit.

D. Benalcazar-Bernevig-Hughes model on $\{6, 4\}$ lattice

The Benalcazar-Bernevig-Hughes (BBH) model [51], originally defined on the square lattice, can be easily generalized to hyperbolic $\{p, 4\}$ lattices with even p as described in the main text for $p = 6$.

1. $\{6, 4\}$ lattice

The $\{6, 4\}$ lattice is defined by the hyperbolic tessellation where four hexagons meet at each vertex, i.e., it is formed by the four-fold rotation symmetric vertices V_y of the Schwarz triangles, cf. Fig. S5. Its space group is the triangle group $\Delta(2, 4, 6)$ and the primitive cell (blue polygon in Fig. S5) is given by the smallest quotient T2.2 of Δ with one of its normal subgroups $\Gamma^{(1)}$ [38]:

$$G = \langle a, b, c \mid a^2, b^2, c^2, (ab)^2, (bc)^4, (ca)^6, (bca^{-1}c^{-1})^2 \rangle, \quad (\text{S64})$$

giving

$$\Gamma^{(1)} = \langle \gamma_1, \gamma_2, \gamma_3, \gamma_4 \mid \gamma_4 \gamma_1 \gamma_3 \gamma_4^{-1} \gamma_3^{-1} \gamma_2^{-1} \gamma_1^{-1} \gamma_2 \rangle \quad (\text{S65})$$

$$= \langle \gamma_1, \gamma_2, \gamma_3, \gamma_4 \mid \gamma_1 \gamma_2 \gamma_3 \gamma_4 \gamma_3^{-1} \gamma_1^{-1} \gamma_4^{-1} \gamma_2^{-1} \rangle. \quad (\text{S66})$$

In Ref. 12, a different presentation was found for this group, with six generators $\gamma_1, \dots, \gamma_6$ and three relators $\gamma_1 \gamma_3 \gamma_5$, $\gamma_2 \gamma_4 \gamma_6$, and $\gamma_1 \gamma_2 \gamma_3 \gamma_4 \gamma_5 \gamma_6$. Substituting $\gamma_5 = \gamma_3^{-1} \gamma_1^{-1}$ and $\gamma_6 = \gamma_4^{-1} \gamma_2^{-1}$ from the first two relators into the third relator, we see that this presentation is equivalent to that found in Eq. (S66).

Using GAP, we have found a normal sequence of translation subgroups $\Gamma^{(m)} \triangleleft \Delta(2, 4, 6)$ via the appropriate quotient groups $G^{(m)} \cong \Delta/\Gamma^{(m)}$ given in Ref. 38: With x, y , and z given in Eq. (S53),

$$\begin{aligned} G^{(1)} = G^{\text{T2.2}} &= \langle a, b, c \mid a^2, b^2, c^2, x^2, y^4, z^6, (yz^{-1})^2 \rangle, \\ G^{(2)} = G^{\text{T5.4}} &= \langle a, b, c \mid a^2, b^2, c^2, x^2, y^4, z^6, zyz^{-1}xy^{-1}z^{-2}x \rangle, \\ G^{(3)} = G^{\text{T9.3}} &= \langle a, b, c \mid a^2, b^2, c^2, x^2, y^4, z^6, zyxzy^2z^{-1}xzy^{-1}, zyz^{-1}yxy^{-1}z^{-1}xy^{-1}z \rangle, \\ G^{(4)} = G^{\text{T33.11}} &= \langle a, b, c \mid a^2, b^2, c^2, x^2, y^4, z^6, xzy^{-1}z(yz^{-1})^2xy^{-1}zy^{-1}z^{-1}y \rangle, \\ G^{(4)} = G^{\text{T65.9}} &= \langle a, b, c \mid a^2, b^2, c^2, x^2, y^4, z^6, y^{-1}z(yz^{-1})^2yxy^{-1}z^2(y^{-1}z)^2, (xzyz^{-1})^2(xy^{-1}z^{-2})^2 \rangle, \end{aligned} \quad (\text{S67})$$

with the corresponding connected symmetric supercells illustrated in Fig. S2c and their triangle group graphs as well as boundary identifications given in the supplementary data and code [53].

2. Benalcazar-Bernevig-Hughes model

The BBH model is defined on the $\{6, 4\}$ lattice with four orbitals on each site, i.e., on the vertices of the hexagons, cf. Fig. S5. The four orbitals labeled by numbers 1 to 4 are coupled cyclically by an on-site term with amplitude $\pm h_0$, where a single one of the four couplings carries a minus sign (dashed magenta line) and the other three a plus sign (solid magenta line), thus encoding a magnetic π -flux through the cycle. If each orbital is assigned to one of the four hexagons meeting at the lattice site, the orbitals on different sites assigned to the same hexagon are again coupled cyclically by a hopping with amplitude $\pm h_1$ (solid green line). To encode π -fluxes through all the rectangles along the bonds of the underlying $\{6, 4\}$ lattice, the green bonds forming a

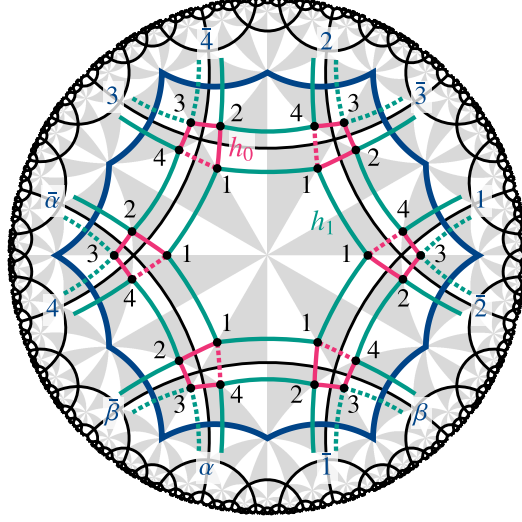


FIG. S5. Definition of the Benalcazar-Bernevig-Hughes model on the $\{6,4\}$ lattice (black lines) and choice of gauge implementing the π -fluxes through the squares and rectangles. There are four orbitals (black dots labeled by black numbers) at each site, coupled by inter-site hoppings $\pm h_0$ (magenta) and intra-site hoppings $\pm h_1$ (green). Dashed lines indicate negative hopping amplitudes. The primitive cell (blue polygon) and its edge identifications are shown: the edge $\bar{1}$ is related to 1 by the translation generator γ_1 ($\bar{\gamma}_1$ for the supercell). Edges related by composite translations are labeled by $\alpha = \gamma_3^{-1}\gamma_1^{-1}$, $\bar{\alpha}, \beta = \gamma_4^{-1}\gamma_2^{-1}$, and $\bar{\beta}$.

hexagon centered at the corner of the primitive cell carry a minus sign. Note that while the chosen gauge does not respect all the symmetries, the physical flux pattern does, cf. Fig. 5 of the main text. This results in the following Hamiltonian

$$\mathcal{H} = h_1 \left[\sum_{\langle i,j \rangle_c} \vec{c}_i^\dagger \begin{pmatrix} 1 & 0 & 0 & 0 \\ 0 & 0 & 0 & 1 \\ 0 & 0 & 0 & 0 \\ 0 & 0 & 0 & 0 \end{pmatrix} \vec{c}_j + \sum_{\langle i,j \rangle_b} \vec{c}_i^\dagger \begin{pmatrix} 0 & 0 & 0 & 0 \\ 0 & 0 & 0 & 1 \\ 0 & 0 & -1 & 0 \\ 0 & 0 & 0 & 0 \end{pmatrix} \vec{c}_j + \text{h.c.} \right] + h_0 \sum_i \vec{c}_i^\dagger \begin{pmatrix} 0 & 1 & 0 & -1 \\ 1 & 0 & 1 & 0 \\ 0 & 1 & 0 & 1 \\ -1 & 0 & 1 & 0 \end{pmatrix} \vec{c}_i, \quad (\text{S68})$$

where $\langle i,j \rangle_c$ denotes NNs within the primitive cell, $\langle i,j \rangle_b$ denotes NNs crossing the boundary of the primitive cell, cf. Fig. S5, and the matrices are given in the basis of orbitals 1, 2, 3, 4 (in that order). As for the other models, we provide the real-space hopping Hamiltonian in graph form in the supplementary data and code [53].

With random sampling of 10^8 (10^6 for T33.11 and T65.9) points in $\mathbb{T}^{2g(m)}$, we have computed the DOS with an energy resolution of $dE = 0.005$ and smoothed using a moving average with window $2dE = 0.01$. The resulting data is shown in Fig. 5b and given as raw data in the supplementary data and code [53].

III. CONVERGENCE OF THE SUPERCELL METHOD

In this section, we provide additional data demonstrating the convergence properties of the supercell method. First, in Section III A, we show the convergence of the density of states (DOS) obtained from a fixed supercell with increasing density of random sampling of the Abelian Brillouin zone (ABZ). We here also observe that for the typical size of the largest supercell considered, the DOS obtained from the spectrum at $\mathbf{k} = 0$ —i.e., the spectrum of the corresponding PBC cluster—does not reproduce the characteristic features of the DOS in the thermodynamic limit; in contrast, the DOS converges rapidly upon the introduction of nontrivial momenta, i.e., under random sampling of the ABZ. Then, in Section III B, we compare the convergence of different normal sequences of supercells, and observe that the DOS appears to converge to the same limit, thereby consolidating our expectation.

A. Convergence with number of points in the Abelian Brillouin zone

Besides allowing a meaningful labeling of eigenstates and therefore simplifying a symmetry analysis [12], one of the main powers of the reciprocal-space description is that it allows us to work with small systems but nevertheless obtain good approx-

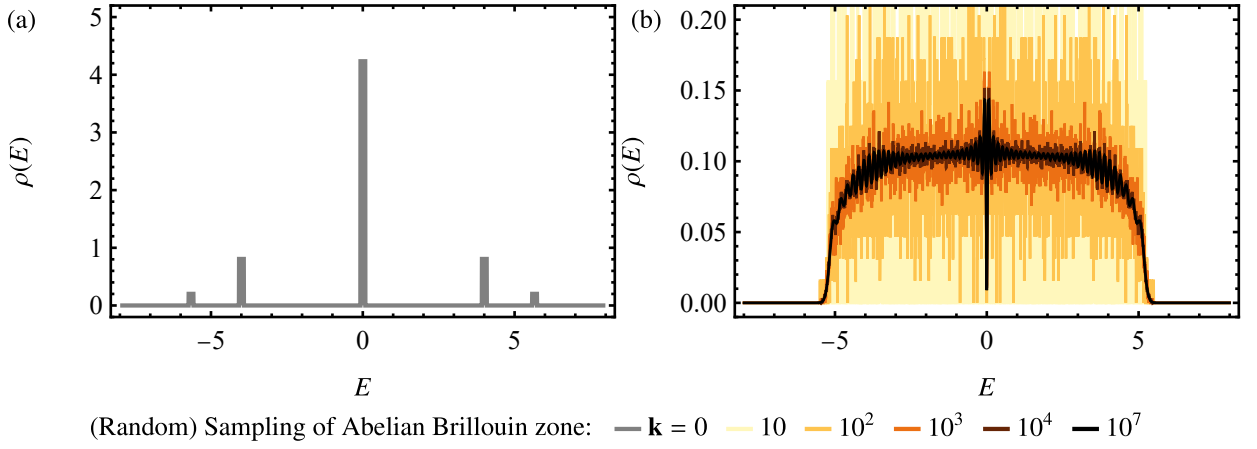


FIG. S6. Convergence of density of states (DOS) of the nearest-neighbor hopping model defined on the 64-supercell T65.78 of the $\{8, 8\}$ lattice. (a) DOS obtained from treating the 64-supercell as a PBC cluster with 64 sites, effectively setting the Abelian momentum $\mathbf{k} = 0$. The data has been obtained with a resolution of $dE = 0.005$ and smoothed with a moving average over windows of width 0.08. (b) DOS obtained from treating the 64-supercell as the unit cell of a large PBC cluster and randomly sampling Abelian momenta. The number of sampled momenta is given in the legend. The data has been obtained with a resolution of $dE = 0.005$ and smoothed with a moving average over windows of width 0.01.

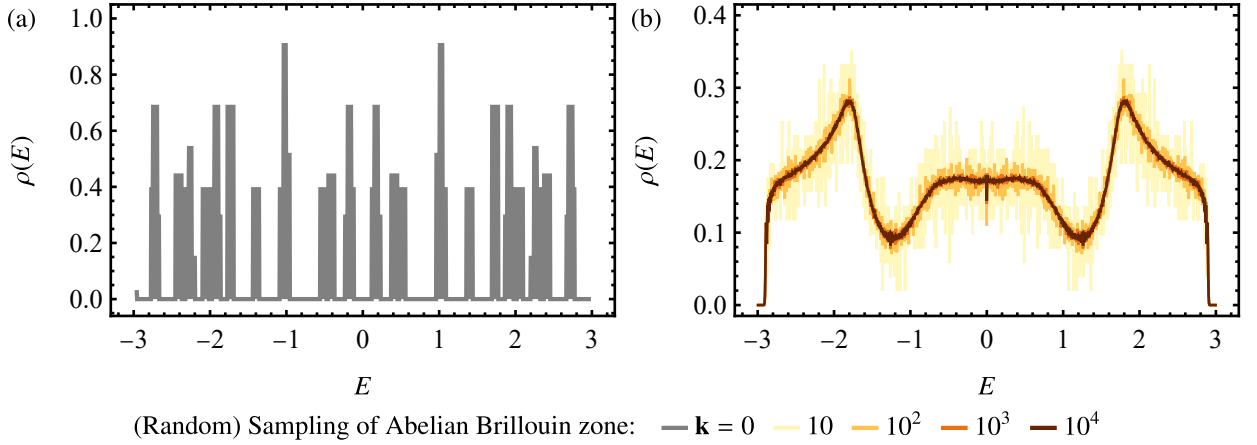


FIG. S7. Convergence of density of states (DOS) of the nearest-neighbor hopping model defined on the 32-supercell T33.1 of the $\{8, 3\}$ lattice. (a) DOS obtained from treating the 32-supercell as a PBC cluster with 512 sites, effectively setting the Abelian momentum $\mathbf{k} = 0$. The data has been obtained with a resolution of $dE = 0.005$ and smoothed with a moving average over windows of width 0.16. (b) DOS obtained from treating the 32-supercell as the unit cell of a large PBC cluster and randomly sampling Abelian momenta. The number of sampled momenta is given in the legend. The data has been obtained with a resolution of $dE = 0.005$ and smoothed with a moving average over windows of width 0.01.

imations of the spectra of larger systems. Formally, Bloch states allow us to approximate models on large PBC clusters, i.e., Eq. (S27) or even its limit for $n \rightarrow \infty$, by diagonalizing only matrices defined on smaller supercells, i.e., Eqs. (S28) and (S49). To demonstrate this power, we compare

- (a) the DOS obtained from treating a given supercell as a PBC cluster in the form of Eq. (S23) with matrix $h_{ij}^{uv}(\gamma) = h^{uv}(\eta_i \gamma \eta_j^{-1})$, which corresponds to evaluating the Abelian Bloch Hamiltonian in Eq. (S49) at $\mathbf{k} = 0$, to
- (b) the DOS obtained from treating the same supercell as a unit cell of a larger PBC cluster, where the same matrix $h_{ij}^{uv}(\gamma)$ appears in Eq. (S41), and randomly sampling the ABZ given in Eq. (S48) with increasing number of sampled points.

Note that (a) is, in essence, the approach of Ref. 35, where the authors diagonalize h_{ij}^{uv} on extremely large PBC clusters whose associated translation groups also form sequences of normal subgroups, albeit different ones from the ones studied here.

In Fig. S6, we show the data described above for the NN model on the supercell T65.78 of the $\{8, 8\}$ lattice. The DOS obtained from simply diagonalizing the 64-site PBC cluster is shown in Fig. S6a and is very far from the converged DOS in Fig. S3a. On

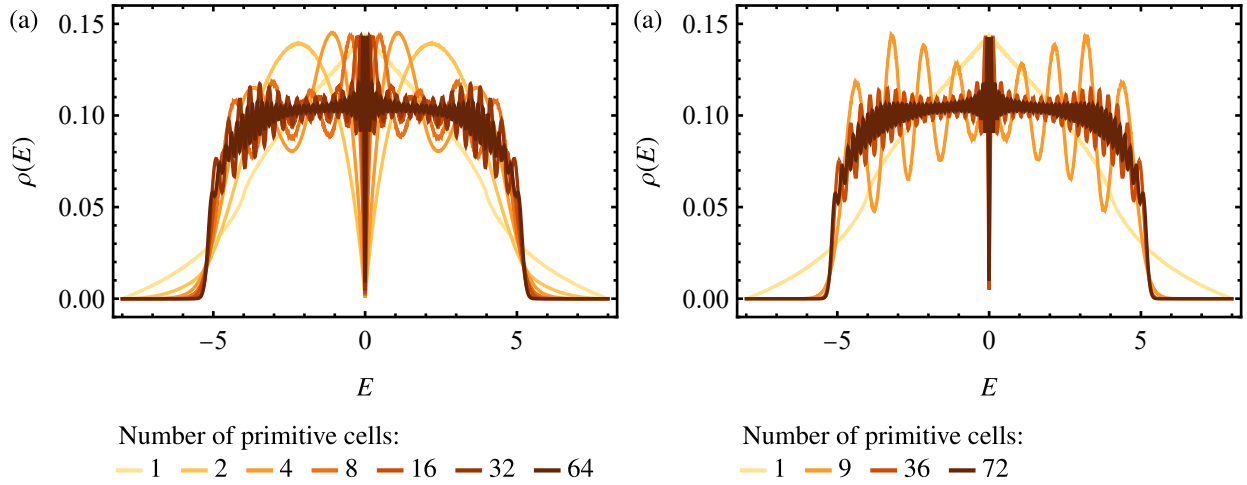


FIG. S8. Density of states of the nearest-neighbor hopping model on the $\{8, 8\}$ lattice [cf. Fig. S3a] for (a) the supercell sequence T2.6, T3.11, T5.13, T9.22, T17.35, T33.58, T65.81 with 1, 2, 4, 8, 16, 32, 64 unit cells per supercell and (b) the sequence T2.6, T10.22, T37.37, T73.71 with 1, 9, 36, 72 unit cells per supercell. In both cases, the energy resolution is 0.005 with a moving average with window 0.01.

the other hand, Fig. S6b shows that upon introducing Abelian momenta, the DOS rapidly converges, with 10^4 (dark red line) randomly sampled points already reproducing most of the features, and 10^7 (black line) being basically indistinguishable from the converged curve shown in Fig. S3a. Note that here we are considering convergence for a *fixed* supercell in the number of sampled momenta, and not in the sequence of supercells; in the latter case T65.78 would be considered not fully converged.

We repeat the same analysis for the NN model on the smaller supercell T33.1 of the $\{8, 3\}$ lattice, which contains $32 \times 16 = 512$ sites, cf. Fig. S7. As for the previous model, the DOS obtained from simply diagonalizing the 512-site PBC cluster is shown in Fig. S7a and is very far from the converged DOS in Fig. S3b. On the other hand, Fig. S7b shows again that upon introducing Abelian momenta, the DOS rapidly converges with 100 (light orange line) randomly sampled points already reproducing most of the features and 10^4 (dark red line) being basically indistinguishable from the converged curve shown in Fig. S3b. A similar convergence can be observed for the Haldane model on the same supercell.

B. Comparison of different supercell sequences

Since the supercell method does not produce unique normal sequences but allows for many different sequences for the same lattice and choice of primitive cell, it remains to be shown that different sequences converge to the same limit. We demonstrate this here using again the NN hopping models on the $\{8, 8\}$ and the $\{8, 3\}$ lattice. For the $\{8, 8\}$ lattice, alternative normal sequences to the one given in Eq. (S54) are [38]

$$\text{T2.6, T3.11, T5.13, T9.22, T17.35, T33.58, T65.81;} \quad (\text{S69})$$

$$\text{T2.6, T10.22, T37.37, T73.71,} \quad (\text{S70})$$

and the corresponding DOS data for 10^7 randomly sampled points in $T^{2g^{(m)}}$ is shown in Figs. S8a and S8b, respectively. Comparing those two figures to Fig. S3a, we observe that they apparently converge to the same limit. For the $\{8, 3\}$ lattice, alternative normal sequences to the one given in Eq. (S59) are [38]

$$\text{T2.1, T5.1, T17.2, T65.1;} \quad (\text{S71})$$

$$\text{T2.1, T10.1, T28.1, T82.1,} \quad (\text{S72})$$

and the corresponding DOS data for 10^7 randomly sampled points in $T^{2g^{(m)}}$ is shown in Figs. S9a and S9b, respectively. Comparing those two figures to Fig. S3b, we again observe apparent convergence to the same limit.

C. Comparison to continued-fraction method

The DOS of the very simple gapless nearest-neighbor hopping models was studied using the continued-fraction method in Ref. 37. We here compare our results obtained for supercells of the $\{8, 8\}$ and $\{8, 3\}$ lattice that contain 72 and 1296 sites,

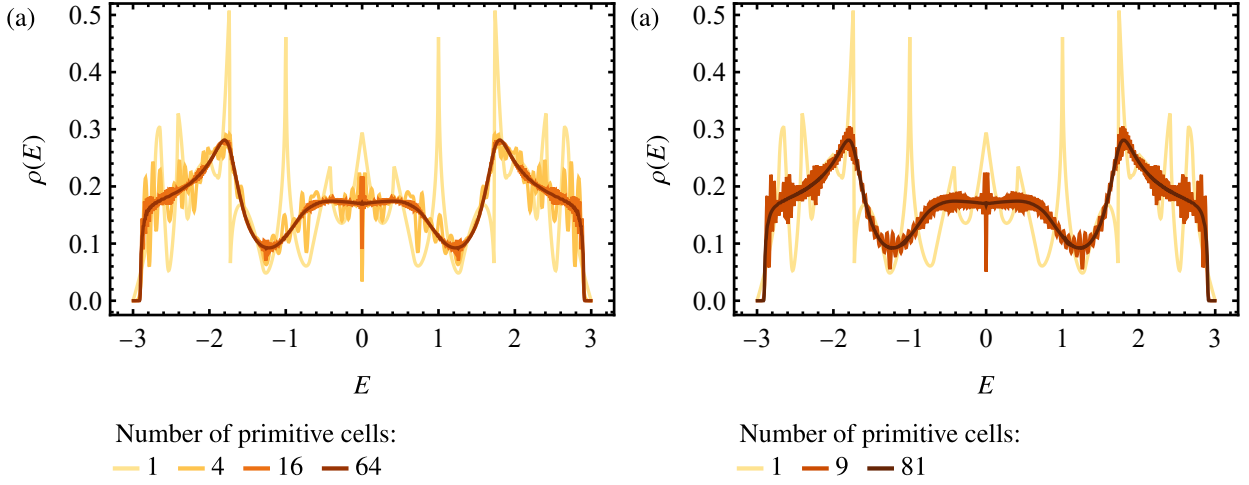


FIG. S9. Density of states of the nearest-neighbor hopping model on the $\{8, 3\}$ lattice [cf. Fig. S3b] for (a) the supercell sequence T2.1, T5.1, T17.2, T65.1 with 1, 4, 16, 64 unit cells per supercell and (b) the sequence T2.1, T10.1, T28.1, T82.1 with 1, 9, 27, 81 unit cells per supercell. In both cases, the energy resolution is 0.005 with a moving average with window 0.01.

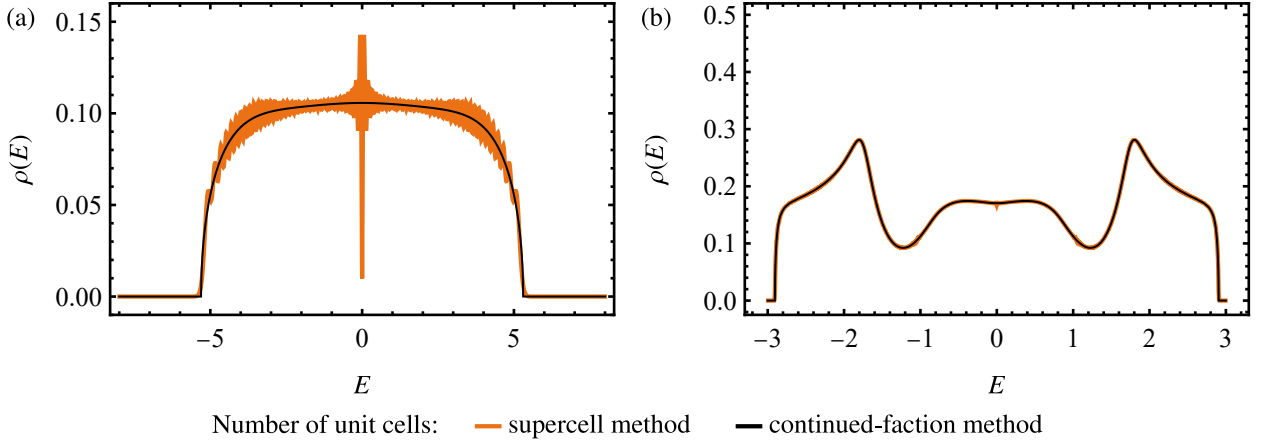


FIG. S10. Density of states of the nearest-neighbor hopping model on (a) the $\{8, 8\}$ lattice and (b) the $\{8, 3\}$ lattice obtained using the supercell method (orange) and the continued-fraction method (black; results from Ref. 37). In (a) the supercell T73.71 with 72 sites and in (b) T82.1 with 1296 sites was used and in both cases, the energy resolution is 0.005 with a moving average with window 0.01.

respectively, to the results of Ref. 37 obtained from more than 10^9 sites. Figure S10 compares the DOS obtained from the two methods and we observe that in both cases the data obtained from the supercell method clearly converges to those obtained using the continued-fraction method. In particular for the $\{8, 3\}$ lattice (Fig. S10b), almost no difference is discernible. On the other hand, our results for the $\{8, 8\}$ lattice are clearly not fully converged (which can be attributed to the much lower number of sites in the corresponding supercell), but the core features are reproduced.

For a more quantitative comparison of the data, we compute the moments of the density of states. The n^{th} moment M_n of $\rho(E)$ is defined as

$$M_n = \int_{-\infty}^{\infty} dE \rho(E) E^n. \quad (\text{S73})$$

Due to the symmetry of the spectra for both the $\{8, 8\}$ as well as the $\{8, 3\}$ lattice, all odd moments vanish. In Tables S1 and S2, we compare the moments obtained from the supercells discussed above to those obtained analytically in Ref. 37. For $\{8, 8\}$, we observe that although the density of states obtained from the 72-site supercell T73.71 is clearly not yet converged (cf. Fig. S10a), the first three even moments are reproduced exactly and the relative error remains below 10^{-4} up to the 16th moment. The accuracy of the odd moments, which should all vanish identically, is similar: the first five odd moments are below 10^{-10} and up to the 15th moment, all of them are below 10^{-4} . For $\{8, 3\}$, Fig. S10b indicates a significantly better level of convergence and we find accordingly that the first seven even moments, i.e., up to the 14th moment, are obtained exactly, while the relative error

Odd moments			Even moments		
n	Supercell	Continued-fraction [37]	n	Supercell	Continued-fraction [37]
1	1.55×10^{-16}	0	2	8	8
3	8.92×10^{-15}	0	4	120	120
5	2.66×10^{-13}	0	6	2 192	2 192
7	7.48×10^{-12}	0	8	44 263	44 264
9	2.02×10^{-10}	0	10	950 582	950 608
11	5.19×10^{-9}	0	12	21 288 185	21 288 912
13	1.45×10^{-7}	0	14	491 503 907	491 515 088
15	3.96×10^{-6}	0	16	11 614 603 543	11 614 244 072
17	1.10×10^{-4}	0	18	279 540 473 553	279 495 834 368
19	2.97×10^{-3}	0	20	6 828 817 799 853	6 826 071 585 040
21	8.18×10^{-2}	0	22	168 891 218 655 925	168 755 930 104 880
23	2.24	0	24	4 220 862 714 087 351	4 214 946 994 935 248

TABLE S1. Odd (left) and even (right) moments of the density of states of the $\{8, 8\}$ lattice obtained from the supercell (based on T73.71 and rounded to the nearest integer) and continued-fraction [37] methods. The numbers given by the latter are exact. For even moments, digits highlighted in orange indicate deviation from the exact result.

Odd moments			Even moments		
n	Supercell	Continued-fraction [37]	n	Supercell	Continued-fraction [37]
1	9.13×10^{-17}	0	2	3	3
3	6.37×10^{-16}	0	4	15	15
5	3.59×10^{-15}	0	6	87	87
7	4.09×10^{-14}	0	8	549	549
9	3.06×10^{-13}	0	10	3 663	3 663
11	2.76×10^{-12}	0	12	25 407	25 407
13	1.80×10^{-11}	0	14	181 233	181 233
15	1.93×10^{-10}	0	16	1 320 119	1 320 117
17	1.47×10^{-9}	0	18	9 772 395	9 772 359
19	1.05×10^{-8}	0	20	73 274 242	73 273 755
21	8.61×10^{-8}	0	22	555 164 111	555 158 277
23	8.27×10^{-7}	0	24	4 242 668 085	4 242 602 877
25	5.30×10^{-6}	0	26	32 660 090 468	32 659 394 745
27	4.82×10^{-5}	0	28	252 987 887 054	252 980 710 305
29	4.28×10^{-4}	0	30	1 970 260 645 697	1 970 188 493 067
31	3.80×10^{-3}	0	32	15 416 884 219 376	15 416 173 400 134
33	2.94×10^{-2}	0	34	121 137 511 606 951	121 130 623 234 816
35	2.21×10^{-1}	0	36	955 367 811 569 773	955 301 961 767 219

TABLE S2. Odd (left) and even (right) moments of the density of states of the $\{8, 3\}$ lattice obtained from the supercell (based on T82.1 and rounded to the nearest integer) and continued-fraction [37] methods. The numbers given by the latter are exact. For even moments, digits highlighted in orange indicate deviation from the exact result.

remains below 10^{-4} for the first 18 even moments. The first seven odd moments are below 10^{-10} and up to the 27th moment, all of them are below 10^{-4} .

Overall, the comparison with the exact moments gives further evidence to the convergence of the supercell method and affirms our expectation that other quantities besides the density of states, where our reciprocal-space perspective can fully manifest its efficacy, will experience similar convergence.